Atmospheric
Chemistry
and Physics

The impacts of secondary ice production on microphysics and dynamics in tropical convection

Zhipeng Qu[1], **Alexei Korolev**[1], **Jason A. Milbrandt**[1], **Ivan Heckman**[1], **Yongjie Huang**[2],
Greg M. McFarquhar[3,4], **Hugh Morrison**[5], **Mengistu Wolde**[6], **and Cuong Nguyen**[6]

[1]Meteorological Research Division, Environment and Climate Change Canada, Toronto, Ontario, Canada
[2]Center for Analysis and Prediction of Storms, University of Oklahoma, Norman, OK, USA
[3]Cooperative Institute for Severe and High-Impact Weather Research and Operations,
University of Oklahoma, Norman, OK, USA
[4]School of Meteorology, University of Oklahoma, Norman, OK, USA
[5]Mesoscale and Microscale Meteorology Laboratory, National Center for Atmospheric Research,
Boulder, CO, USA
[6]National Research Council Canada, Ottawa, Canada

Correspondence: Zhipeng Qu (zhipeng.qu@ec.gc.ca)

Abstract. Secondary ice production (SIP) is an important physical phenomenon that results in an increase in the ice particle concentration and can therefore have a significant impact on the evolution of clouds. In this study, idealized simulations of a mesoscale convective system (MCS) were conducted using a high-resolution (250 m horizontal grid spacing) mesoscale model and a detailed bulk microphysics scheme in order to examine the impacts of SIP on the microphysics and dynamics of a simulated tropical MCS. The simulations were compared to airborne in situ and remote sensing observations collected during the "High Altitude Ice Crystals – High Ice Water Content" (HAIC-HIWC) field campaign in 2015. It was found that the observed high ice number concentration can only be simulated by models that include SIP processes. The inclusion of SIP processes in the microphysics scheme is crucial for the production and maintenance of the high ice water content observed in tropical convection. It was shown that SIP can enhance the strength of the existing convective updrafts and result in the initiation of new updrafts above the melting layer. Agreement between the simulations and observations highlights the impacts of SIP on the maintenance of tropical MCSs in nature and the importance of including SIP parameterizations in models.

1 Introduction

Secondary ice production (SIP) is recognized as a fundamental cloud microphysical process (e.g., Cantrell and Heymsfield, 2005; Field et al., 2017). Production of secondary ice involves processes that require the presence of pre-existing ice particles. SIP is different from primary ice production (PIP), which commences by the nucleation of ice either homogeneously in strongly supercooled droplets or heterogeneously on the surface of ice-nucleating particles (INPs) (e.g., Kanji et al., 2017).

The first in situ observations of SIP go back to the early 1960s (e.g., Murgatroyd and Garrod, 1960; Koenig, 1963, 1965). Multiyear in situ measurements have shown that SIP is an very common phenomenon, and it occurs in different types of clouds from polar regions to the tropics; these findings are based on recent SIP studies including Lloyd et al. (2015), Lawson et al. (2015, 2017), Lasher-Trapp et al. (2016), Keppas et al. (2017), Mignani et al. (2019), Korolev and Leisner (2020), Li et al. (2021), Luke et al. (2021), and many others.

The primary effect of SIP is the enhancement of the ice particle concentration that, depending on environmental conditions, may exceed the concentration of PIP ice particles by several orders of magnitude (e.g., Hobbs and Rangno, 1985; Ladino et al., 2017). Such an enhancement of the ice particle concentration may have a significant effect on the phase composition, cloud dynamics, precipitation rate, and cloud radiative properties, impacting the energy balance and hydrological cycle on regional and global scales.

At present, seven mechanisms are recognized as sources of secondary ice in clouds. These include the fragmentation of freezing droplets (hereafter FFD; e.g., Kleinheins et al., 2021), rime splintering (i.e., the Hallett–Mossop process, hereafter HM; e.g., Hallett and Mossop, 1974), fragmentation due to ice–ice collisions (e.g., Vardiman 1978; Takahashi et al. 1995), ice fragmentation due to thermal shock (e.g., Dye and Hobbs, 1968), fragmentation of sublimating ice (Oraltay and Hallett, 1989), activation of INPs in transient supersaturation around freezing drops (e.g., Prabhakaran et al., 2020), and break-up of freezing water drops on impact with ice particles (James et al., 2021). A detailed description of the first six SIP mechanisms and the status of associated laboratory studies are discussed in the review by Korolev and Leisner (2020). It was found that HM and FFD are the most experimentally studied SIP mechanisms, as well as the mechanisms for which production rates of secondary ice have been quantified. However, a detailed analysis of previous experiments by Korolev and Leisner (2020) revealed a large diversity of the ice production rates, which led to the conclusion that these SIP processes need to be studied further. The other four mechanisms have a limited number of laboratory experiments, and they cover only a fraction of environmental conditions (e.g., fragmentation during ice collisions and fragmentation of sublimating ice) or only demonstrate the general feasibility of SIP mechanisms (e.g., fragmentation due to thermal shock and activation of INPs in transient supersaturation around freezing drops). All of the above-mentioned information led Korolev and Leisner (2020) to the conclusion that the relative contributions of each of the six SIP mechanisms in the enhancement of ice concentrations remain uncertain.

Over the last few years, there have been many new efforts based on systematic studies of the effect of SIP on cloud microphysics with the help of cloud simulations (e.g., Phillips et al., 2017, 2018; Sullivan et al., 2018; Hoarau et al., 2018; Fu et al., 2019; Sotiropoulou et al., 2020, 2021; Dedekind et al., 2021; Hawker et al., 2021; Huang et al., 2021, 2022; and others). Most of these modelling efforts have been focused on matching simulated moments of particle size distributions (PSDs) with those observed in situ. In many ways, the implementation of SIP in numerical models has been hindered by the lack of consensus on the parameterizations of SIP mechanisms.

One of the main objectives of this work is to identify and simulate the occurrence of high ice water content (IWC) associated with the enhancement of ice particle concentrations from SIP processes. Cloud environments with high IWC ($> 1\,\mathrm{g\,m^{-3}}$) pose a hazard for civil aviation and may result in engine power loss, stall, or damage (e.g., Lawson et al., 1998; Mason et al., 2006; Mason and Grzych, 2011). The phenomenon of high IWC has been well documented from in situ observations in tropical mesoscale convective systems (MCSs) (e.g., Heymsfield and Palmer, 1986; Lawson et al., 1998; Gayet et al., 2012; Fridlind et al., 2015; Leroy et al., 2017; Strapp et al., 2021). Several previous modelling studies using different cloud microphysical parameterizations have attempted to reproduce high IWCs. Ackerman et al. (2015) used a 1D model to explore microphysics in tropical MCSs. Simulations performed with 3D models (Franklin et al., 2016; Stanford et al., 2017; Qu et al., 2018) pointed to inaccuracies in the estimation of cloud PSD, IWC, and ice category compared with the observations. Huang et al. (2021) conducted high-resolution simulations of tropical convection and found significant overestimates of radar reflectivity and underestimates of total ice crystal concentration (N_i). Adding SIP in high-resolution simulations, Huang et al. (2022) found a significant improvement in simulated N_i compared with the in situ observations.

In most of the previous numerical studies investigating SIP, the microphysics schemes used were based on the traditional approach of representing ice-phase hydrometeors by partitioning them into various predefined categories (e.g., pristine ice, snow, and graupel) with prescribed physical properties. This approach has several inherent limitations and problems, including a limited range of ice properties (e.g., bulk density) that can be represented, inconsistent physical processes applied to the categories, and the need to parameterize conversion between categories – an artificial process which can not be constrained from observations and is purely ad hoc. To address this problem, Morrison and Milbrandt (2015) proposed a new approach and developed a new microphysics parameterization – the Predicted Particle Properties (P3) scheme – whereby all ice-phase hydrometeors are represented by a single "free" ice category whose physical properties evolve continuously. While flexible in this regard, one limitation of the original P3 scheme was that it could not represent more than one population of ice particles (with different bulk properties) at a given time and grid location. Thus, the scheme was generalized to allow for a user-specified number of "free" ice categories, each of which have properties that evolve continuously and can represent any ice type (Milbrandt and Morrison, 2016).

The P3 scheme was used in the tropical convection simulations of Huang et al. (2022). While they found that adding three SIP mechanisms significantly improved simulated N_i compared with the in situ observations, their simulations were limited to two ice categories. This is the minimum number of categories required for including SIP processes, as at least two categories are needed to represent the coexistence of newly formed small ice splinters and pre-existing large ice

particles. However, as will be shown below, the use of more than two ice categories may be beneficial or even necessary to model the impacts of SIP in deep convection.

This study is focused on the examination of the effects of SIP on the microphysics and dynamics of a simulated tropical MCS. Quasi-idealized simulations of a MCS were conducted using a near-cloud-resolving configuration (250 m horizontal grid spacing) of a 3D dynamical model with the P3 microphysics scheme. Model configurations with up to four free ice categories were tested. The enhancement of the ice particle concentration by SIP is represented by the HM and FFD mechanisms. In the absence of a consensus on SIP parameterizations, these two processes were described by two specific parameterizations proposed in the literature, which provide a sufficient enhancement of N_i above the melting layer consistent with in situ observations in the MCSs (Korolev et al., 2020). Simulated ice PSD, N_i, IWC, radar reflectivity, and Doppler velocity were compared against in situ and remote sensing observations collected during the "High Altitude Ice Crystals – High Ice Water Content" (HAIC-HIWC) field campaign in 2015 (Strapp et al., 2021). Without looking for an exact match between model simulations and observations, this study aimed to show whether the simulation with SIP produces a better estimation of the observed microphysics compared with the simulation without SIP.

The remainder of the paper is structured as follows. Section 2 describes the observational data used for evaluation. In Sect. 3, the set-up of the model, the microphysics scheme, and the parameterizations of SIP are detailed. Section 4 describes the choice of control simulation with regard to the number of ice categories in P3. Section 5 assesses the impact of SIP on the formation of ice clouds based on the control simulation. The role of SIP in strengthening and sustaining tropical convection is discussed in Sect. 6. This is followed by an assessment of the impact of the ice–ice collection efficiency on the simulation (Sect. 7). Section 8 offers a summary of the study and conclusions.

2 Observational data

In situ data employed in this study were collected from the National Research Council of Canada (NRC) Convair 580 and Service des Avions Français Instrumentés pour la Recherche en Environnement (SAFIRE) Falcon 20 research aircraft. The coordinated flight operations of the NRC Convair 580 and the SAFIRE Falcon 20, in the framework of the HAIC-HIWC campaign, were performed out of Cayenne (French Guiana) during May 2015.

The measurements of PSDs were performed by three particle probes that covered different particle size ranges: the Droplet Measurement Technologies (DMT) Cloud Droplet Probe (CDP: Lance et al., 2010) was used for measurements of droplets in the $2\,\mu m < D < 50\,\mu m$ size range; the Stratton Park Engineering Company (SPEC) 2D imaging (stereo)

instrument (2D-S: Lawson et al., 2006) covered the nominal size range from 10 to 1250 μm; and the DMT Precipitation Imaging Probe (PIP: Baumgardner et al., 2001) provided measurements of particles in the nominal size range from 100 μm to 6.4 mm (PSD). The processing software employed a retrieval algorithm of partially viewed particle images (Heymsfield and Parrish, 1979; Korolev and Sussman, 2000), which allowed the enhancement of particle statistics and extended the maximum size of the composite PSD up to 12.8 mm.

All particle probes were equipped with anti-shattering tips to mitigate the effect of ice shattering on the measurements of the ice particle concentration. Residual shattering artefacts were identified and filtered out with the help of the inter-arrival time algorithm (Field et al., 2006; Korolev and Field, 2015).

The bulk IWC was measured by an isokinetic probe (IKP: Davison et al., 2008). The IKP allowed measurements of IWC up to $10\,g\,m^{-3}$ at the aircraft speed of $200\,m\,s^{-1}$. Such a high upper limit of IWC well exceeded the maximum IWC ($\sim 5\,g\,m^{-3}$) measured during the HAIC-HIWC campaign and ensured that the measured IWC never exceeded the IKP saturation level.

Both aircraft were equipped with the same instruments for measurements of PSDs and bulk IWC and used the same processing algorithms applied to these measurements. This arrangement minimized differences in systematic errors specific to different types of instruments and synchronized data processing. Therefore, if any potential biases in data acquisition and data processing existed, they would be the same for both data sets collected from the NRC Convair 580 and the SAFIRE Falcon 20.

Besides comparisons with IWC and N_i, model results are also compared with reflectivity and Doppler velocity measured by the NRC aircraft X-band radar (NAX) installed on the NRC Convair 580 (Wolde and Pazmany 2005). Statistics of the NAX data included the MCS cloud segments that precipitated down to the ground surface level. Cloud segments with outflow cirrus that had radar returns disconnected from the ground were excluded from the statistics.

3 Model configuration

3.1 Atmospheric model and initialization

The model used in this study is the Global Environmental Multiscale (GEM) model (Côté et al., 1998; Girard et al., 2014). The GEM model is used for operational numerical weather prediction (NWP) by Environment and Climate Change Canada (ECCC) as well as research at ECCC and Canadian universities. The dynamical core of GEM is formulated based on the non-hydrostatic fully compressible primitive equations with a terrain-following hybrid vertical grid. As such, it can be run at cloud-resolving (sub-kilometre grid spacing) scales. It can be run on global or limited-area do-

Table 1. Summary of the GEM model configurations' details. References to specific schemes are provided in Milbrandt et al. (2016).

Dynamics/numerics

– Non-hydrostatic primitive equations
– Limited-area grid on a latitude–longitude projection
– Uniform horizontal grid spacing of 0.00225 longitude (approximately 0.25 km)
– 82 vertical levels
– Upper-boundary nesting above 10 hPa
– Time step of 15 s
– Terrain-following Gal-Chen vertical coordinate
– Two-time-level semi-implicit time differencing
– 3D semi-Lagrangian advection
– ∇^4 horizontal diffusion (∇^6 for potential temperature)

Physics

– Planetary boundary layer scheme based on turbulence kinetic energy with statistical representation of subgrid-scale cloudiness (MoisTKE)
– Kuo transient shallow convection scheme
– P3 two-moment bulk microphysics scheme
– Li–Barker correlated-k distribution radiative transfer scheme (called every 3 min)
– Interaction Sol–Biosphère–Atmosphère (ISBA) land surface scheme
– Distinct roughness lengths for momentum and heat/humidity

mains and is capable of one-way nesting. In this study, an idealized model configuration was used to simulate tropical deep convection, with a horizontal grid spacing of 250 m in a simulation domain of 160 km × 160 km, with 83 vertical levels over a tropical ocean surface. The horizontal grid spacing of 250 m is nearly at the cloud-resolving scale (Bryan et al., 2003; Lebo and Morrison, 2015). It is also close to the corresponding distances (110 to 180 m) of the 1 Hz in situ observational data from the aircraft which flew mostly at 110–120 m s^{-1} (Convair 580) and 150–180 m s^{-1} (Falcon 20). To resolve the vertical profiles near the tropical melting layer, vertical grid spacings of approximately 100 m were used between the altitudes of 4 and 7.5 km. The reader is referred to Table 1 for more details on the dynamics/numerics and physics configurations used in the model.

The atmospheric initial conditions were horizontally homogeneous, based on an initial sounding taken from the operational global GEM analysis at 12:00 UTC on 15 May 2015 at 6.769° N, 49.551° W. The initial profile (Fig. 1) had 1697 J kg^{-1} of convective available potential energy (CAPE). The GEM analysis also provided the initial sea surface temperature. The location and time were chosen based on the occurrence of an extensive mesoscale system that formed in this region and was observed (Fig. 2) during the HAIC-HIWC field campaign (Strapp et al., 2021).
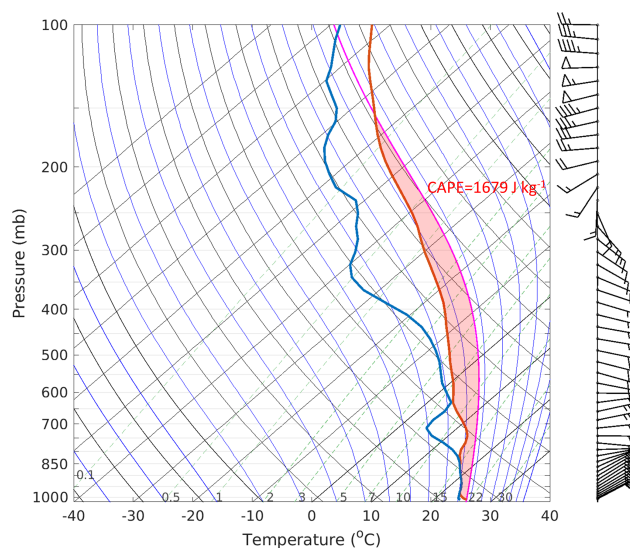
Figure 1. Initial atmospheric profiles for the idealized simulations. The blue line represents the dew point temperature, the red line represents the environment sounding (temperature), and the magenta line represents the parcel lapse rate.

To initiate the model storm, the updraft nudging method of Naylor and Gilmore (2012) was used to force convection during the first 15 min of the simulation. Three distinct updrafts were initialized 15 km apart from each other in the western part of the simulation domain. Each updraft was forced by perturbing the vertical air velocity (w_t) in a spheroid with a horizontal radius of 10 km and vertical radius of 1.5 km, centred at 1.5 km altitude, as shown in Eqs. (1) and (2).

$$w_{\text{mag}} = \begin{cases} w_{\text{max}}\cos^2\left(\frac{\pi}{2}\beta\right) & \text{if } 0 \leq \beta \leq 1, \\ 0 & \text{if } \beta > 1. \end{cases} \tag{1}$$

$$w_t = w_{t-1} + \text{dts} \times \alpha \times \max(w_{\text{mag}} - w_{t-1}, 0). \tag{2}$$

Here, β is the distance from the centre of the spheroid normalized by its radius, α is an inverse nudging timescale (0.5 s^{-1}), dts is the model time step, and w_{max} is the maximum updraft speed (10 m s^{-1}) for nudging.

3.2 Cloud microphysics scheme

All cloud microphysical processes in the GEM simulations were represented by the P3 two-moment bulk microphysics scheme, where up to four (free) ice categories were used. For each ice category, there are four prognostic (i.e., advected) mixing ratio variables: the total ice mass, the rime mass, the bulk volume, and the total number. From the prognostic variable fields, various bulk physical properties can be computed. The size distribution of each category is represented by a complete gamma function. The liquid-phase component of P3 consists of two-moment categories for cloud droplets and rain. For details on the representation of each hydrometeor category and the parameterized microphysical processes, the

reader is referred to Morrison and Milbrandt (2015); for details on the multi-category configuration, see Milbrandt and Morrison (2016).

It should be noted that there have been several further key developments to P3 since the first version of the multi-ice-category scheme, along with various minor modifications. Major developments include a triple-moment treatment of rain (Paukert et al., 2019), the introduction of a prognostic liquid fraction for wet ice (Cholette et al., 2019), and a triple-moment treatment of ice (Milbrandt et al., 2021). The version of P3 used in this study does not include these major modifications. The impacts of these components of P3 on SIP may be examined in future work. It is possible, for example, that triple-moment ice, which in principle results in a better representation of the PSD dispersion, may be important for some aspects of modelling SIP and its impacts. However, such work is outside of the scope of this study.

3.3 Parameterization of SIP

The following two SIP mechanisms were examined in this study. Other mechanisms will be considered in the future.

3.3.1 Rime splintering/Hallett–Mossop (HM)

The pristine version of P3 used in this study (i.e., prior to the SIP-related modifications examined here) includes a parameterization of the HM mechanism if two or more ice categories are used. The requirement for at least two categories is to prevent the dilution of ice particle properties when two populations of ice are forced to be represented by a single size distribution and set of physical properties (see Milbrandt and Morrison, 2016). The parameterized HM process produces a maximum of 350 ice crystals per milligram of collected liquid water, with crystal sizes of 10 μm, during riming of rain within a temperature range of $-3\,°C > T > -8\,°C$, with the peak value at $-5\,°C$ and varying linearly to 0 ice crystals per milligram at the extreme temperature ranges. This ice multiplication parameterization has been used in several traditional (fixed-ice-category) microphysics schemes (e.g., Reisner et al., 1998). This is similar to the original HM parameterization in P3 as used in Milbrandt and Morrison (2016).

One modification to the HM parameterization in this study is to exclude the use of collected liquid water from the situation where raindrops ($100\,\mu m < D < 3500\,\mu m$) were collected/nucleated by small ice particles ($D < 100\,\mu m$). From the point of view of the SIP mechanism, it is more appropriate to apply this part of collected liquid water to the FFD mechanism.

3.3.2 Fragmentation of freezing drops (FFD)

The parameterization of the FFD mechanism was implemented following Lawson et al. (2015):

$$N_f = 2.5 \times 10^{-11} D^4, \tag{3}$$

where N_f is the average number of ice fragments per drop, and D is the drop diameter in micrometres. The parameterization of the FFD process was applied for raindrops ($100\,\mu m < D < 3500\,\mu m$) that were nucleated by ice particles ($D < 100\,\mu m$). Following Keinert et al. (2020), the activity of the FFD process was limited to the temperature range of $-25\,°C < T < -2\,°C$. Within the temperature range, the current parameterization is not dependent on temperature. Further studies are being undertaken in order to explore the impacts of variation due to temperature.

3.3.3 Ice collection efficiency

Although not directly part of SIP, ice aggregation is another process that impacts N_i and may therefore be important in affecting high IWC. There are several different approaches to parameterize the ice collection efficiency, which is a key parameter in the aggregation parameterization (Hallgren and Hosler, 1960; Lin et al. 1983; Cotton et al., 1986; Ferrier et al., 1994, 1995; Milbrandt and Yau, 2005a, b; Seifert and Beheng, 2006). Khain and Pinsky (2018) showed that the collection efficiencies in these parameterizations vary by more than 2 orders of magnitude for any given temperature between -40 and $0\,°C$. Sensitivity simulations conducted in the framework of this current study showed a high sensitivity of the modelled IWC and N_i to the collection efficiency of ice. The collection efficiency used in this study follows Cotton et al. (1986). Further discussion of the sensitivity of the modelling results to the ice aggregation parameterization is presented in Sect. 7.

4 Establishment of the control configuration

The number of ice categories used in the P3 scheme can impact the overall simulation results (Milbrandt and Morrison, 2016). SIP results in large quantities of small ice splinters, which can be co-located with pre-existing larger ice particles; thus, bimodal or multi-modal ice size distributions may occur. This cannot be represented with the single-ice-category configuration because P3 uses complete gamma size distributions for each hydrometeor category. Therefore, SIP – or any other ice initiation process – could result in the "dilution" of the bulk particle properties of existing ice where the microphysics scheme tries to represent two or more populations of ice particles within a single size distribution and with a single set of bulk physical properties (e.g., mean size). Thus, before examining the impacts of SIP in the simulation, a control configuration must be established based on the minimum number of ice categories needed to represent ice particle evolution in P3 with sufficient detail. This is determined by the number of categories beyond which adding more does not change the simulated average profiles for more than 15% of the fields of interest (e.g., IWC and N_i). To address this, a series of sensitivity tests was conducted (1) using the baseline version of P3 (with no SIP) and varying the number of
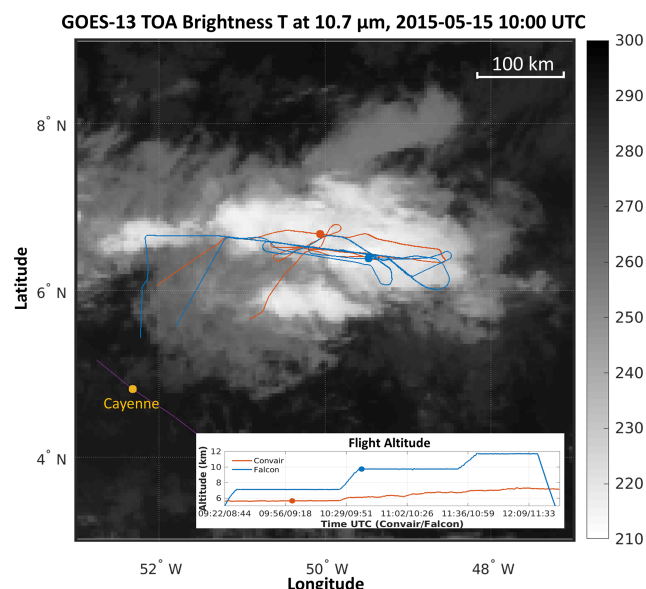
Figure 2. GOES-13 top-of-atmosphere (TOA) brightness temperature at 10.7 µm at 10:00 UTC on 15 May 2015 (Knapp et al., 2018). Blue lines denote the Falcon 20 flight track and altitudes; red lines denote the Convair 580 flight track and altitudes; red and blue dots indicate the locations and altitudes of the Convair 580 and Falcon 20 aircraft, respectively, at 10:00 UTC; and purple line represent the coastline.

ice categories from one to four and (2) using P3 with SIP included and varying the number of categories from two to four.

Table 2 summarizes the complete list of experiments conducted in this study. For the experiments starting with "BASE" (denoting the baseline P3 configuration), no SIP is activated. The experiments starting with "SIP" use the new parameterization for both the FFD and HM process. In the following analysis, we focus on the simulation results between 90 and 150 min, when the convective systems are more complex and more closely resemble the observed MCS.

As described in Sect. 3, three convective cells were initiated in the eastern part of the simulation domain. Figure 3 shows the upward longwave flux from the BASE-1ICE simulation at the top of the atmosphere (Fig. 3a, b, c, d) and the radar reflectivity of the vertical cross sections (Fig. 3e, f, g, h) indicated by black lines in Fig. 3a–d for simulation times of 30, 60, 120, and 180 min. The initial formation of the three convective updrafts can still be seen at 30 min (Fig. 3a). By 60 min, these updrafts started to merge, forming a larger system (Fig. 3b). This system then moved westward (towards the right of the domain) and developed into a sustained system (Fig. 3c). By 180 min, the convection began to weaken (Fig. 3d, h).

Figure 4 shows averaged profiles for the baseline simulations with different numbers of ice categories. The mean profiles of IWC (Fig. 4a) and N_i (Fig. 4b) consider all points

with IWC larger than $0.001\,\mathrm{g\,m^{-3}}$. The maximum vertical wind speed (w_{max}; Fig. 4c) and average temperature profiles (Fig. 4d) apply to the entire model domain. The mean rain-water profiles are calculated based on data from the atmospheric columns in which both the ice water path and rain water path are larger than $1\,\mathrm{g\,m^{-2}}$ (Fig. 4e). The radar reflectivity profiles (Fig. 4f) are the median values including points with either IWC or rain water content (RWC) larger than $0.01\,\mathrm{g\,m^{-3}}$ within the mask used for Fig. 4e.

For the altitude range between 5 and 12 km, adding one more ice category to the one-, two-, and three-category baseline simulations produces maximal changes of 12 %, 23 %, and 7 % for IWC, respectively (Fig. 4a). Similarly, maximal changes of 25 %, 31 %, and 14 % are found for N_i (Fig. 4b). The radar reflectivity (Fig. 4f) for the one-ice-category run (BASE-1ICE) is about 4 to 6 dBZ lower than the three- or four-category simulations in the same altitude range. This is likely caused by the fact that a single ice category is not sufficient to represent the coexistence of large and small ice particles and results in a reduction of the concentration of large ice particles, leading to lower radar reflectivity. With regard to the number of ice categories for SIP simulations, a similar conclusion to the baseline simulations was found. Adding one more ice category to two- and three-category SIP simulations produces maximal changes of 31 % and 9 % for IWC, respectively (Fig. 5a). For N_i, maximal respective changes of 70 % and 15 % are found (Fig. 5b). Therefore, at least three ice categories in P3 appear to be necessary and sufficient to examine the impacts of including SIP processes. Note that adding more ice categories for baseline and SIP simulations will not significantly change the morphology of the storm. It is of passing interest to note that the similarity of the three- and four-ice category results is consistent with the 1D kinematic simulations in Milbrandt and Morrison (2016). However, given that the use of more ice categories in P3 is generally preferable in principle (although there is added computational cost) and that four-ice-category simulations were already performed, BASE-4ICE is taken as the control run for the sensitivity studies to follow; this simulation is referred to as CTR. Correspondingly, we focus on the four-ice-category simulation including SIP (SIP-4ICE) for direct comparison to CTR.

5 Impacts of SIP on microphysical properties

5.1 Domain-averaged profiles

Figure 6 shows simulated average profiles for the four-ice-category simulation including SIP processes – SIP-4ICE (see Table 2) – as well as for CTR. As seen in Fig. 6a, the SIP-4ICE simulation has at least 100 % higher IWC compared with the control run above 6 km. SIP-4ICE has significantly higher N_i than CTR (Fig. 6b), with differences reaching 2–3 orders of magnitude near 6 km and about 1 order of magnitude above 11 km.

Table 2. List of simulations.

Experiment name	Coalescence efficiency between ice particles	Number of ice categories	Secondary ice production (SIP)
BASE-1ICE	Cotton et al. (1986)	One	No SIP
BASE-2ICE		Two	
BASE-3ICE		Three	
BASE-4ICE (CTR)		Four	
BASE-COL	Linear from 0.1 to 1.0 between -20 and $-5\,°C$, 0.1 below $-20\,°C$, and 1.0 above $-5\,°C$	Four	
SIP-2ICE	Cotton et al. (1986)	Two	Droplet shattering: large rain droplet ($100\,\mu m < D < 3500\,\mu m$) collected by small ice particle ($D < 100\,\mu m$) Hallett–Mossop: applied to the remaining collected rain by ice
SIP-3ICE		Three	
SIP-4ICE		Four	
SIP-COL	Linear from 0.1 to 1.0 between -20 and $-5\,°C$, 0.1 below $-20\,°C$, and 1.0 above $-5\,°C$	Four	

Figure 3. Simulation with a single ice category in the P3 bulk microphysics scheme for **(a–d)** upward longwave radiative flux at the top of atmosphere at four different times (30, 60, 120, and 180 min after the model initiation), and **(e–h)** the corresponding radar reflectivity of the cross section marked by the black line in panels **(a)–(d)**.

Figure 6c shows the maximum vertical air velocity in the domain. The simulations are very similar below the melting layer ($\sim 4.5\,km$), but the w_{max} of SIP-4ICE is 2 to $5\,m\,s^{-1}$ higher above the melting layer. This suggests that SIP enhances convection due to the sudden production of a large number of small ice particles, resulting in the rapid freezing of rainwater and depletion of water vapour by diffusional growth. Both effects result in latent heating, which invigorates convection. This can be inferred from Fig. 6e, which shows that RWC in CTR is reduced from $0.12\,g\,m^{-3}$ at $4.2\,km$ to $0.05\,g\,m^{-3}$ at $5\,km$, whereas RWC from SIP-4ICE is changed from $0.12\,g\,m^{-3}$ at $4.2\,km$ to $0.01\,g\,m^{-3}$ at

$5\,km$. Another potential mechanism of convection enhancement above the melting layer will be discussed in Sect. 6.

The medians of radar reflectivity of the SIP simulation is 5 to $10\,dBZ$ lower compared with those of the CTR simulation between the altitudes of 5 and $12\,km$ (Fig. 6f). This is because the SIP simulation has smaller ice particles, despite the higher IWC values, due to the higher N_i.

In order to confirm that the simulation differences illustrated in Fig. 6 are indeed the result of the inclusion of parameterized SIP processes, and not simply a chance set of changes that could result from perturbations in the model due to some minor code change, a set of 10 ensemble simulations
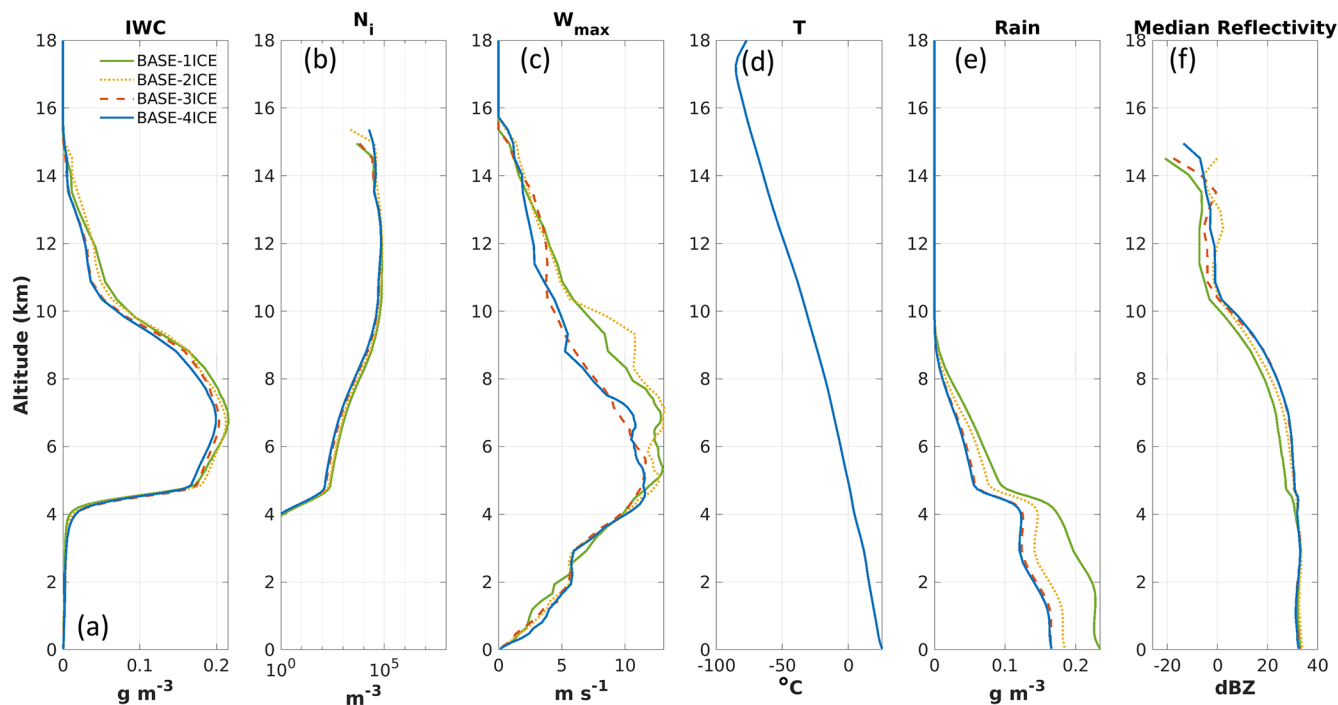
Figure 4. Profiles from the baseline simulations without SIP for (**a**) ice water content (IWC), (**b**) ice number concentration (N_i), (**c**) maximum vertical wind speed (W_{max}), (**d**) air temperature (T; the four simulations have only slightly different temperature that is not distinguishable in the figure), (**e**) rain water content (RWC), and (**f**) median radar reflectivity. The profiles are calculated based on data from 90 to 150 min of simulation. Panels (**a**) and (**b**) are horizontally averaged over regions with IWC $> 0.001\,\mathrm{g\,m^{-3}}$, panel (**c**) is the horizontal maximum across the domain, panel (**d**) is a horizontal average over the whole domain, panel (**e**) is an average over the area with both ice water path and rain water path larger than $1\,\mathrm{g\,m^{-2}}$, and panel (**f**) shows median values of reflectivity including points with either IWC or RWC larger than $0.01\,\mathrm{g\,m^{-3}}$ within the mask used for panel (**e**).
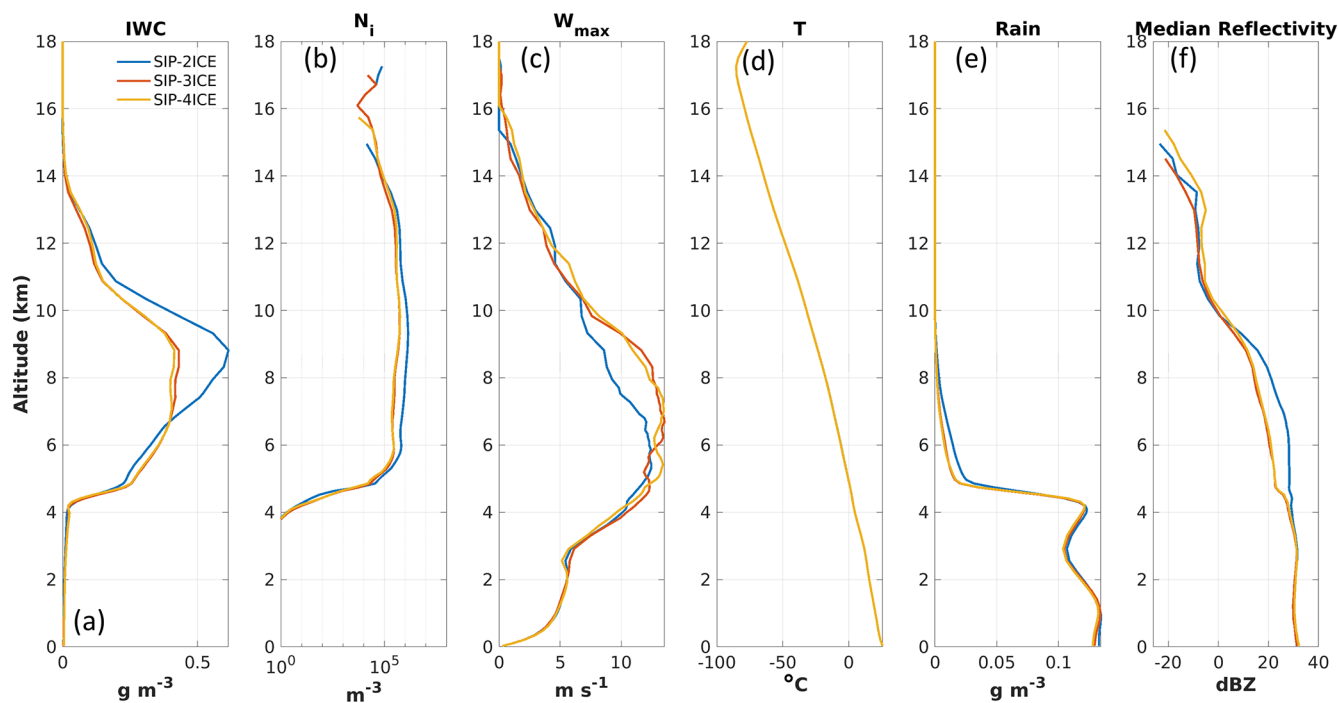
Figure 5. Same as Fig. 4 but for the SIP simulation with two, three, and four ice categories.
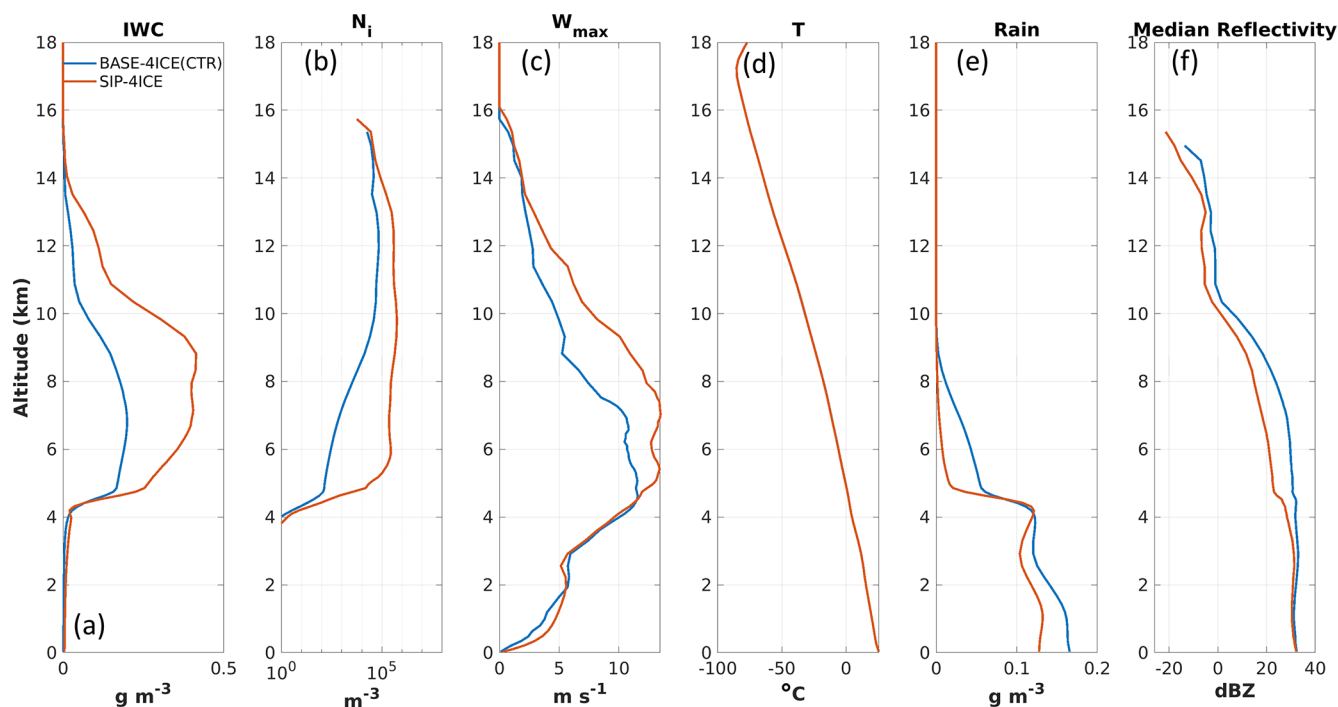
Figure 6. Same as Fig. 4 but for the baseline (CTR) simulation with four ice categories and the SIP simulation with four ice categories.

were run for each configuration (CTR and SIP-4ICE) but with perturbed initial conditions. Figure 7 shows the ensemble results for the two configurations at 120 min. Each configuration includes 11 members (1 unperturbed and 10 perturbed members). The initial temperature profile is randomly perturbed with the maximum range of $\pm 1\,°C$ at all model levels. The ensemble results show high consistency. The SIP simulation consistently produces much higher IWC and N_i. The vertical velocity w_{max} of an ensemble member is the single maximal value of a given model level. Therefore, the profiles of w_{max} can be noisy. The ensemble profiles of w_{max} for CTR and SIP-4ICE overlap, especially below the altitude of $\sim 6\,km$. However, the averaged maximal vertical velocity w_{max} (solid lines) diverges above the altitude of $\sim 6\,km$, which indicates that the SIP simulations generate stronger updrafts in general. The RWC and the radar reflectivity are both strongly reduced by 5 to 10 dBZ in the SIP simulations between 5 and 10 km. Similar remarks can be made for all other times between 90 and 150 min (not shown). The results summarized in Fig. 7 lend support to the idea that the differences between CTR and SIP-4ICE are indeed due to the effects of SIP on the microphysical and thermodynamic fields and are not merely another model realization of a chaotic weather system.

5.2 Ice number concentration

Figure 8 shows comparisons of the probability density function of N_i, $F(N_i)$, calculated from the simulations and mea-

sured during airborne in situ observations at two different altitude (H) ranges. The N_i measured in situ is calculated for the size range between 40 µm and 12.5 mm. The ice particles smaller than 40 µm are not counted due to large uncertainty of the instrument in that size range (Baumgardner et al., 2017). The $F(N_i)$ values measured in situ were averaged over all HAIC-HIWC flights for the clouds with IWC $> 0.01\,g\,m^{-3}$. Figure 8a shows a comparison of $F(N_i)$ at altitudes $6 < H < 7\,km$. The CTR simulation (blue line) shows a significant underestimation of N_i compared with the measured values (black line). The concentrations corresponding to the modal value of $F(N_i)$ in CTR are nearly 2 orders of magnitude lower than those obtained from in situ observations. The SIP-4ICE simulation (red line) shows good agreement with the measured values.

The general behaviour of the functions $F(N_i)$ for $11 < H < 12\,km$ (Fig. 8b) is similar to that obtained for $6 < H < 7\,km$ in Fig. 8a. The maxima of $F(N_i)$ for CTR and observed values correspond to approximately the same ice concentrations of $10^5\,m^{-3}$. However, the maximum of $F(N_i)$ in CTR is nearly triple that of the observed $F(N_i)$ which was reasonably close to that of SIP-4ICE. The width of $F(N_i)$ from SIP-4ICE agrees better with the observations than that from CTR. There are almost no grid points in CTR with a concentration above $\sim 3 \times 10^5\,m^{-3}$, whereas SIP-4ICE overestimated $F(N_i)$ compared with the measured values. The overestimation of N_i of around $3 \times 10^5\,m^{-3}$ is probably caused by uncertainty in the parameterizations of both the FFD process and the ice–ice collection efficiency.
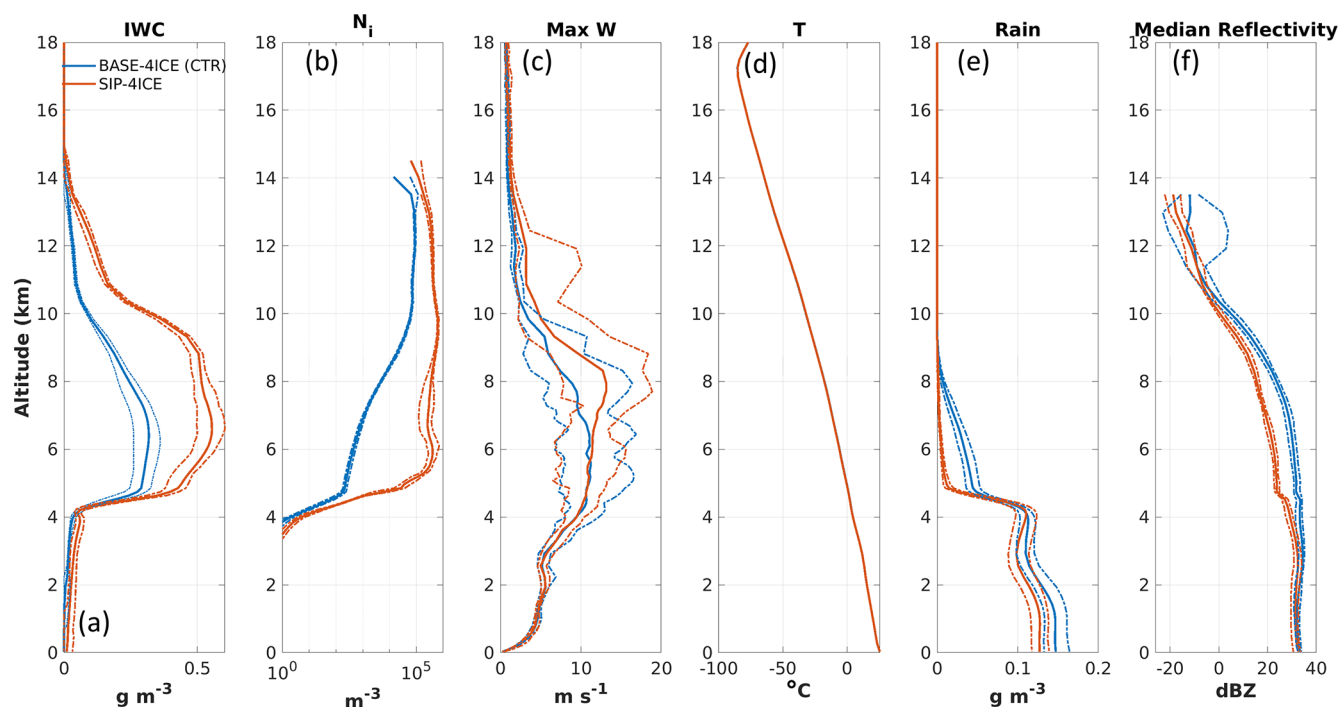
Figure 7. Same as Fig. 4 but showing the domain-averaged profiles for the CTR and SIP simulations with four ice categories, for 11 ensemble members each. The dot-dash lines show the minimum and maximum values among the ensemble members. The results are calculated based on data at 120 min after the model initiation.
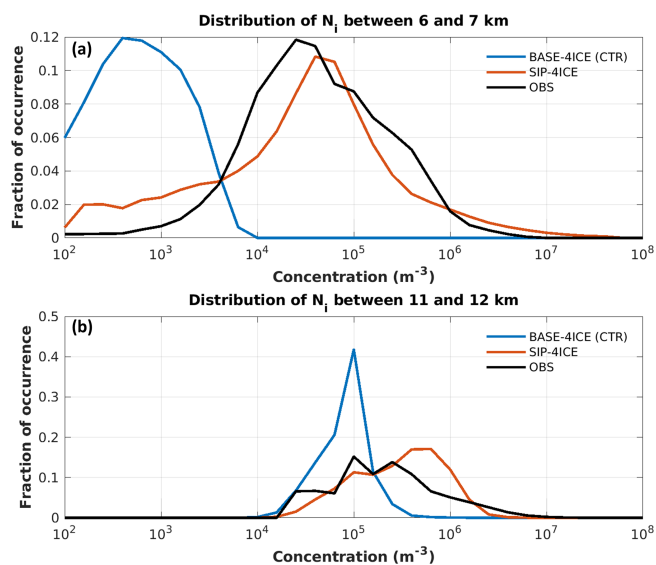

Figure 8. Distribution of N_i for model simulations and for the observational data from the HAIC-HIWC aircraft campaign near French Guiana in May 2015. A logarithmic bin width of 1/5 of an order of magnitude is used. Panel **(a)** displays results from data between altitudes of 6 and 7 km and with an ice water content higher than $0.01 \, \mathrm{g \, m^{-3}}$. Panel **(b)** is the same as panel **(a)** but for altitudes between 11 and 12 km.

This warrant further studies on better quantifications of both processes.

5.3 Ice water content

Similar to the results discussed above, Figure 9 shows comparison of probability density functions of the IWC, $F(\mathrm{IWC})$, obtained from model simulations and aircraft observations at altitudes $6 < H < 7 \, \mathrm{km}$ (Fig. 9a) and $11 < H < 12 \, \mathrm{km}$ (Fig. 9b). As seen in Fig. 9a, $F(\mathrm{IWC})$ from SIP-4ICE is in good agreement with the observations for IWC values smaller than $3.25 \, \mathrm{g \, m^{-3}}$. In contrast, the simulated frequency of encountering high IWC values in CTR is about 1/2 to 1/500 of the observed frequency between an IWC of 1 and $2 \, \mathrm{g \, m^{-3}}$. There are no data with IWC values higher than $2.5 \, \mathrm{g \, m^{-3}}$ in CTR.

SIP-4ICE produces some points with IWC $> 3.25 \, \mathrm{g \, m^{-3}}$, which were not observed by the instruments. The $F(\mathrm{IWC})$ of these high IWC conditions from SIP-4ICE are below 1.7×10^{-5}. For the Convair 580 aircraft, the number of observed 1 s average data points with IWC $> 0.01 \, \mathrm{g \, m^{-3}}$ is 59 893. This sets the limit of $F(\mathrm{IWC})$ of the observational data at 1.7×10^{-5}. If the campaign lasted much longer, it is conceivable that these high-IWC conditions might have eventually been observed.

Figure 9b shows similar results but for higher altitudes (between 11 and 12 km). The frequency of IWC values between 0.3 and $1.3 \, \mathrm{g \, m^{-3}}$ in CTR is about 2–3 orders of magni-
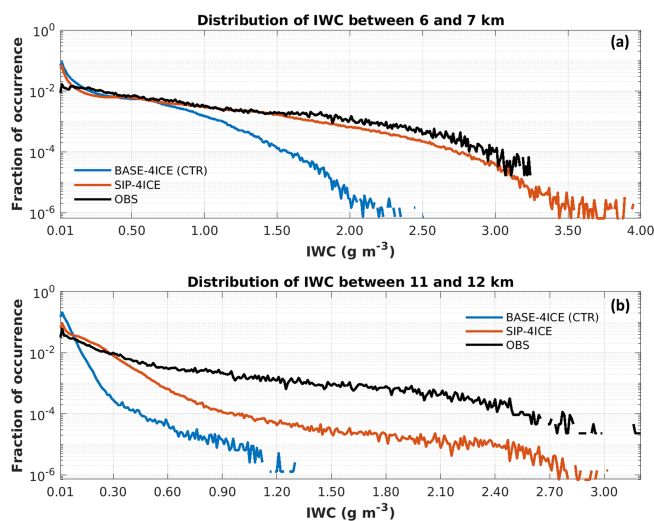
Figure 9. Distributions of ice water content (IWC) from the model simulations and observational data from the HAIC-HIWC aircraft campaign near French Guiana in May 2015. The bin width of $0.01\,\mathrm{g\,m^{-3}}$ is used. Panel **(a)** displays results from between altitudes of 6 and 7 km and with observational data from the NRC Convair 580 aircraft, and panel **(b)** presents results between altitudes of 11 and 12 km and with the observational data from the SAFIRE Falcon 20 aircraft.

tude lower than the observed frequency. There are no data with IWC values higher than $1.30\,\mathrm{g\,m^{-3}}$ from CTR. SIP-4ICE produces closer estimates compared to the observational data, as they both have IWC values up to $\sim 3\,\mathrm{g\,m^{-3}}$. Between 11 and 12 km, N_i of SIP-4ICE is considerably improved compared with CTR, as shown in Fig. 8b. However, the IWC of SIP-4ICE at these altitudes is still underestimated by 1–2 orders of magnitude beyond an IWC of $0.7\,\mathrm{g\,m^{-3}}$ compared with the observation. One possible reason for this underestimate is the differences in the sampling of data. At higher altitudes, between 11 and 12 km, there are often extensive areas with thin ice clouds near the convection. The data from SIP-4ICE used in the statistics include these areas if the IWC of the grid cell is larger than $0.01\,\mathrm{g\,m^{-3}}$. In contrast, the HAIC-HIWC campaign targeted conditions with a high IWC. The thinner ice clouds with IWC values between 0.01 and $0.3\,\mathrm{g\,m^{-3}}$ might not have been sufficiently sampled, as they are less relevant to the extreme conditions causing safety issues for aviation. This difference might partly explain the higher $F(\mathrm{IWC})$ below $0.3\,\mathrm{g\,m^{-3}}$ and the lower $F(\mathrm{IWC})$ above $0.3\,\mathrm{g\,m^{-3}}$ for SIP-4ICE compared with the observations. Another possible explanation of the underestimation is the uncertainty in the strength of simulated convections. In this study, the maximal updraft nudging speed $w_{\max} = 10\,\mathrm{m\,s^{-1}}$ is used as the default value. Simulations with different $w_{\max}$ values are also tested. Using $w_{\max} = 15\,\mathrm{m\,s^{-1}}$ in the SIP-4ICE simulation will produce a 63 % higher averaged IWC between 10 and 11 km than that produced by the default SIP-4ICE simulation with

$w_{\max} = 10\,\mathrm{m\,s^{-1}}$. For the SIP-4ICE simulation, the impact of $w_{\max}$ for lower altitudes between 6 and 7 km is negligible. The CTR simulation with $w_{\max} = 15\,\mathrm{m\,s^{-1}}$ produces a higher IWC compared with the default CTR simulation with $w_{\max} = 10\,\mathrm{m\,s^{-1}}$ (20 % and 50 % higher for altitudes range of 6–7 and 10–11 km, respectively). However, these values are still significantly smaller than those of the default SIP-4ICE simulation.

5.4 Longwave radiation and radar reflectivity

Figure 10 shows the upward longwave radiative flux at the top of atmosphere (TOA) for three different simulation times (90, 120, and 150 min) from CTR (Fig. 10a, b, c) and SIP-4ICE (Fig. 10d, e, f). The lowest TOA flux of SIP-4ICE is on average 11.4 °C lower than that of CTR. The surface of area with TOA longwave flux lower than $170\,\mathrm{W\,m^2}$ for SIP-4ICE is on average 2.7 times larger than that of CTR. This suggests that the cloud tops with SIP included are higher (Fig. 10d, e), and the anvil clouds are more extensive (Fig. 10e, f).

The corresponding simulated radar reflectivity of the cross section indicated by the black lines in Fig. 10 is shown in Fig. 11. One significant difference between the CTR (Fig. 10a, b, c) and SIP-4ICE (Fig. 10d, e, f) simulations is that the reflectivity from the simulation with SIP is significantly lower than that of the control run between altitudes of approximately 5 and 10 km. This is due to the higher N_i values and, thus, smaller ice particle sizes in SIP-4ICE.

Figure 12 shows a comparison of the frequency distribution of radar reflectivity for CTR and SIP-4ICE (Fig. 12a, b) and for the NRC Convair 580 X-band radar (Fig. 12c). For the results of the two simulations, only the atmospheric columns with both ice water path and rain water path values larger than $1\,\mathrm{g\,m^{-2}}$ are selected. The X-band radar data in Fig. 12c were averaged over all research flights during the HAIC-HIWC campaign. Figure 12d shows the simulated and observed median values of the reflectivity. At altitudes higher than 10.3 km, reflectivity in both the CTR and SIP-4ICE runs is lower than the measured reflectivity. However, between 5 and 10 km, SIP-4ICE has values closer to the observations, with a maximum overestimation of 4 dBZ at 5 km. CTR clearly overestimates the reflectivity by 5 to 15 dBZ between 5 and 10 km.

For SIP-4ICE between 5 and 8 km, there is a large number of cases with reflectivity larger than 25 dBZ; this is not found in the observations. Figure 13 shows the comparison of N_i and IWC against reflectivity for CTR (Fig. 13a, b), SIP-4ICE (Fig. 13c, d), and the observations (Fig. 13e, f). Although the distributions of N_i and IWC simulated using SIP-4ICE are closer to the observations than those of CTR, a significant number of cases (35.8 %) from SIP-4ICE still have reflectivity values larger than 25 dBZ, whereas only 0.4 % of the observations are above 25 dBZ.

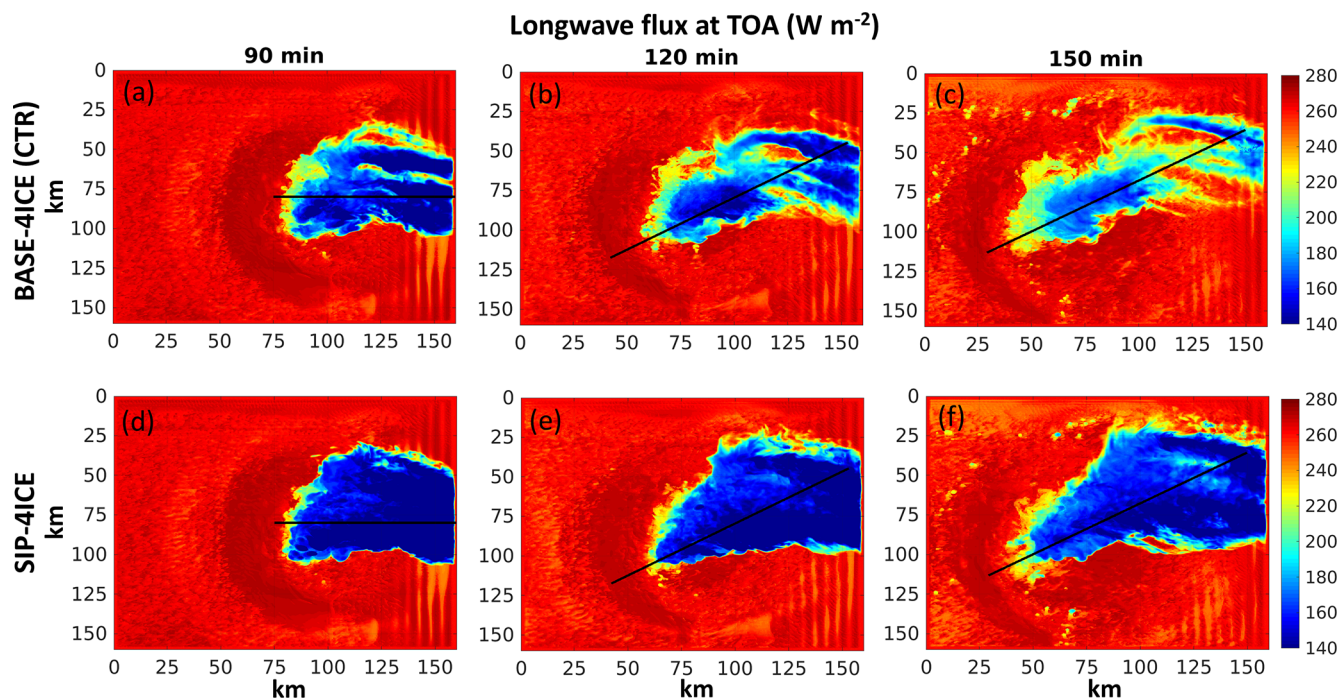Figure 14 shows the 2D histograms for the IWC and reflectivity (Fig. 14a, b, c, d) and for the N_i and reflectiv-

Longwave flux at TOA (W m⁻²)

Figure 10. Longwave flux at the top of atmosphere for **(a–c)** the simulation with the baseline GEM set-up with four free categories of ice at 60, 120, and 180 min after the initiation. Panels **(d)**– **(f)** are the same as panels **(a)**– **(c)** but for the simulation with SIP implemented. Black lines indicate the location of the cross sections shown in later results.
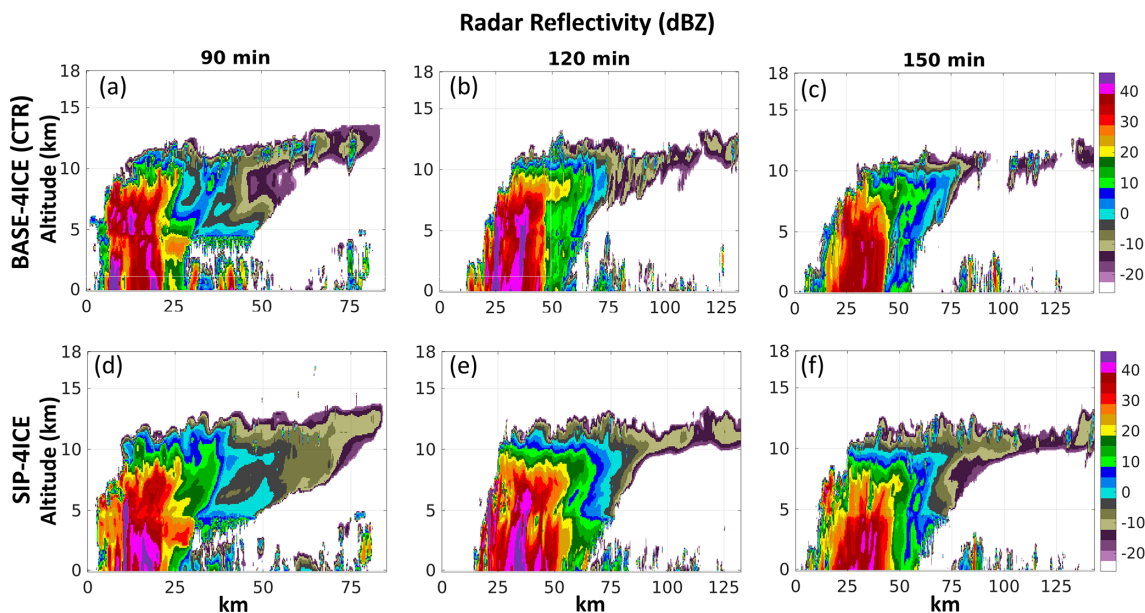
Radar Reflectivity (dBZ)

Figure 11. Simulated radar reflectivity for the cross sections indicated by the black lines in Fig. 10.

ity (Fig. 14e, f, g, h) for each of the four ice categories in SIP-4ICE. The ice categories 1 and 3 have generally lower reflectivity (1 % and 3 % higher than 25 dBZ, respectively) and higher N_i (peak value at $10^{4.4}$ and 10^4 m^{-3}, respectively). By contrast, ice categories 2 and 4 have higher reflectivity (23 % and 24 % higher than 25 dBZ, respectively) and lower N_i

(peak value at $10^{3.4}$ and $10^{2.8}$ m^{-3}, respectively). This means that the ice particles in categories 2 and 4 have much larger mean sizes than those of categories 1 and 3. Most of the ice particles in categories 2 and 4 with reflectivity larger than 25 dBZ are lightly rimed aggregated ice with a rime fraction of ~ 20 %. The mean-mass diameter of these ice particles
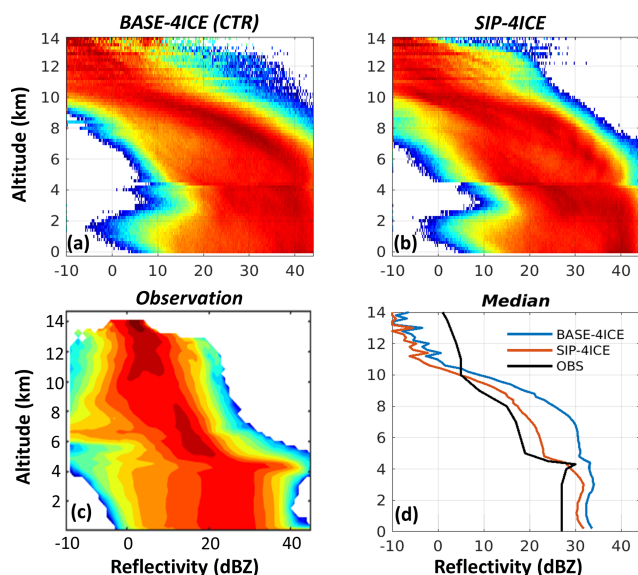
Figure 12. Radar reflectivity distribution frequency for **(a)** CTR with four ice categories between 60 and 180 min after model initiation. Panel **(b)** is the same as panel **(a)** but for the model with SIP included. Panel **(c)** is from all of the observational data from the NRC Convair 580 aircraft during the HAIC-HIWC campaign. Panel **(d)** is the median value for each altitude for the two model simulations and observations.

could reach several millimetres. It is probable that the high reflectivity values (above 25 dBZ) are the result of these large ice sizes.

Several possible reasons could explain the high reflectivity in the model simulation. Firstly, the model might overproduced large ice particles due to an excessively large ice–ice collection efficiency (which is a highly uncertain parameter). Despite the important role of the ice–ice collection process in clouds, there is no consensus in the scientific literature on how to quantify it. A further discussion on the impact of the ice–ice collection efficiency on the simulation results is presented in the Sect. 7. Secondly, the current P3 version uses a diagnostic shape parameter for the gamma size distribution of ice. The shape parameter, which is a measure of the relative spectral dispersion, might give a wide distribution that implies too many large ice particles and, hence, higher reflectivity. Note that higher moments such as reflectivity are more sensitive to the tail of the size distribution. The triple-moment version of P3 (Milbrandt et al., 2021) uses a prognostic shape parameter that, in principle, should give better size distributions for those large ice particles. However, this comparison is beyond the scope of the current study, as the triple-moment version of P3 was not yet available when this current study began. Finally, the P3 scheme uses a Rayleigh scattering approach to calculate the radar reflectivity. It is not an advanced instrument simulator that can consider the attenuation, multiple and Mie scattering, etc. For the X-band radar on Convair 580, ice particles of several millimetres in size are in a

transition region between Rayleigh and Mie scattering that is not symmetric but has a stronger forward-scattering lobe. Therefore, simulating the radar reflectivity with a Rayleigh scattering approach might overestimate the reflectivity for large ice particles. The radar reflectivity is a useful indicator to understand the model performance; however, considering that a rigorous instrument simulator is not used in this study, it is better to be cautious with regard to the comparison with the reflectivity.

Note that, at the altitude of the melting layer (~ 4.5 km), none of the simulations reproduce the distinct bright band that is clearly apparent in the observational data. This is due to the fact that the version of P3 used in this study does not properly represent the transition state of melting ice with a wet surface and ice core (nor does P3 artificially boost the reflectivity contribution from ice during melting in order to mimic a bright-band effect). As mentioned in Sect. 3.3, a newer version of P3 includes a prognostic variable for the liquid mass content for each ice-phase category that allows for mixed-phase particles and a corresponding improvement in the calculation of reflectivity in the melting zone (which is to be shown in a forthcoming publication).

5.5 Vertical Doppler velocity

The Doppler velocity from the simulation is calculated using the mass-weighted fall speed of all hydrometeors subtracted from the vertical wind speed. Figure 15 shows the simulated Doppler velocity for CTR and SIP-4ICE for the vertical cross section shown in Fig. 11. The Doppler velocity below the melting layer is mostly negative due to the high fall speed of the rain. Above the melting layer, the average Doppler velocity gradually increases from -2 to $0\,\mathrm{m\,s^{-1}}$ with altitude between 5 and 14 km. The gradual increase in the Doppler velocity is primarily linked to the size of ice particles. Positive values of the Doppler velocity are associated with convective cloud regions where the updraft velocity exceeds the falls speed of the ice particles. One difference between the control and SIP simulations is that the SIP-4ICE simulation has a higher Doppler velocity between 5 and 8 km for all three times analyzed.

Figure 16 shows similar results to Fig. 12 but for the Doppler velocity. To mitigate the effect of anvils, the diagrams in Fig. 16a and b used the same mask as that for radar reflectivity in Fig. 12a and b. Both CTR (Fig. 16a) and SIP-4ICE (Fig. 16b) show distribution patterns very similar to those obtained from the observations (Fig. 16c). Figure 16d shows comparisons of the simulated and observed median values of the Doppler velocity vs. altitude. The SIP-4ICE simulation produces very close results to the measurements between the altitude of 5 and 9 km with maximum difference of $\pm 0.3\,\mathrm{m\,s^{-1}}$. The CTR simulation overestimates the negative Doppler velocity by approximately $0.9\,\mathrm{m\,s^{-1}}$ compared with the measured values over the same range of altitudes. This result is consistent with the systematic underestimation
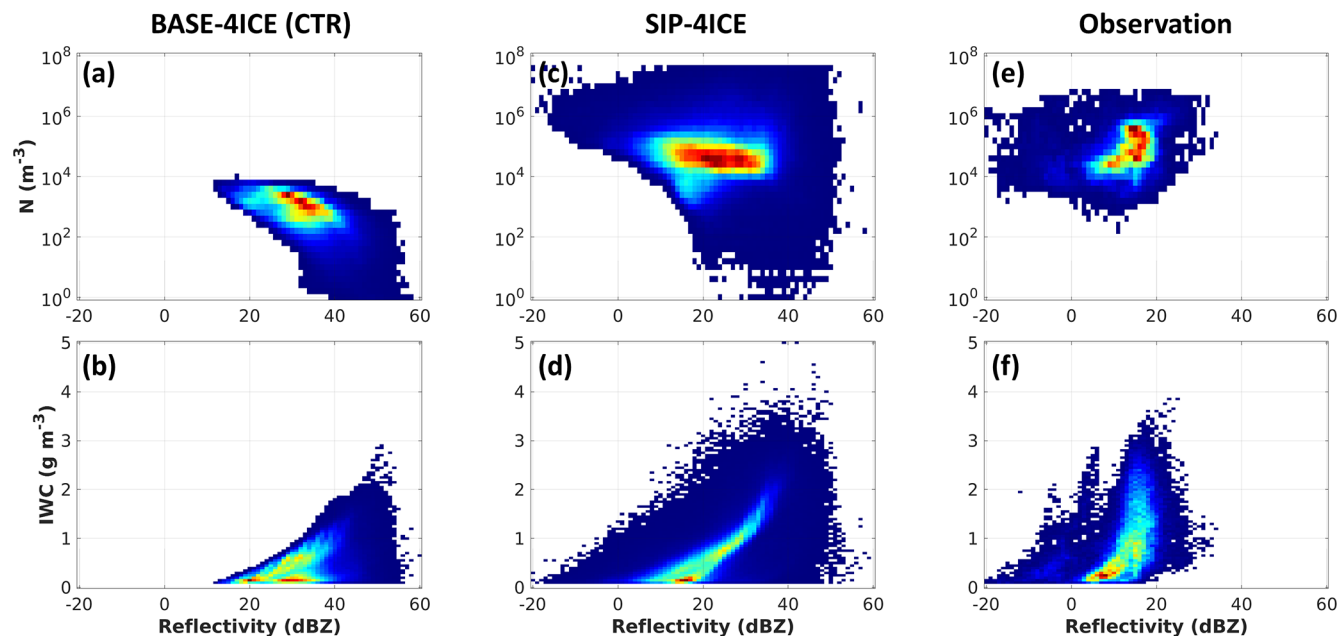
Figure 13. A 2D histogram of N_i and reflectivity (**a, c, e**) and of IWC and reflectivity (**b, d, f**). Panels (**a**) and (**b**) show BASE-4ICE (CTR), panels (**c**) and (**d**) show SIP-4ICE, and panels (**e**) and (**f**) show observations. The data between altitudes of 6 and 7 km are used. For the model simulation, the data between 90 and 150 min are used. The radar reflectivity data from the Convair 580 are the averaged values of the closest upward- and downward-pointing measurements.
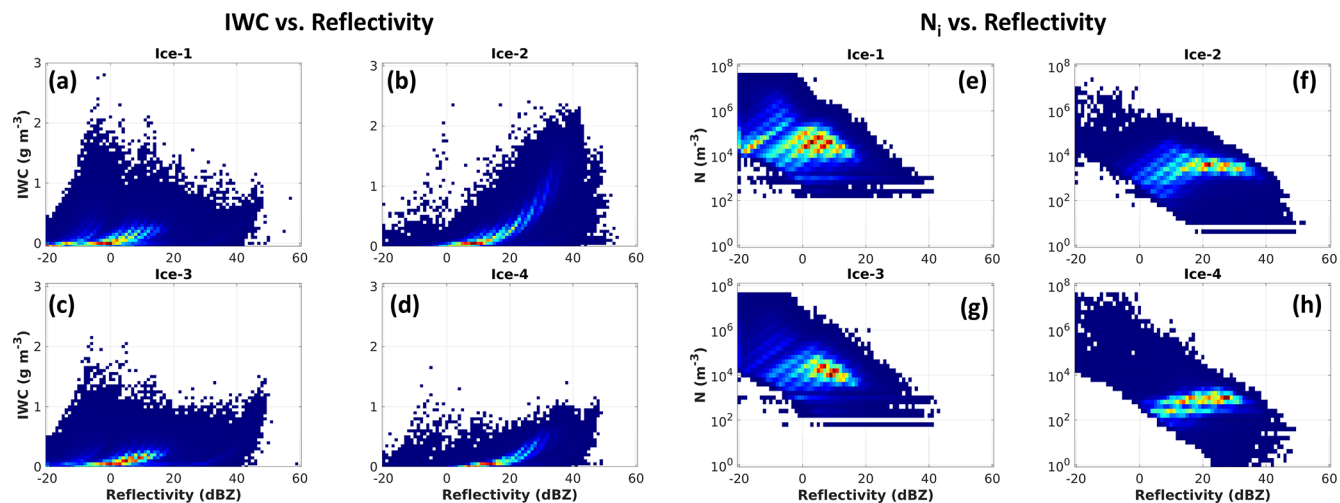

Figure 14. A 2D histogram of IWC and reflectivity (**a–d**) and of N_i and reflectivity (**e–h**) for each of the four ice categories. All results are for the SIP-4ICE simulation between 6 and 7 km and between 90 and 150 min.

of N_i in CTR and, therefore, overestimation of the mean particle sizes and fall speeds.

6 The role of SIP in tropical convection

In the previous section, it was shown that w_{max} is higher in the SIP-4ICE simulation than in the control simulation above the melting layer (Fig. 6c) and that the inclusion of SIP results in the enhanced formation of high-IWC regions above

the melting layer. Altogether these results suggest that SIP plays an important role in the microphysics and thermodynamics of tropical convection, at least for the MCS examined. In order to explore SIP impacts in more detail, the rates and locations of SIP within the model storm and initiation of secondary convection are analyzed in this section.
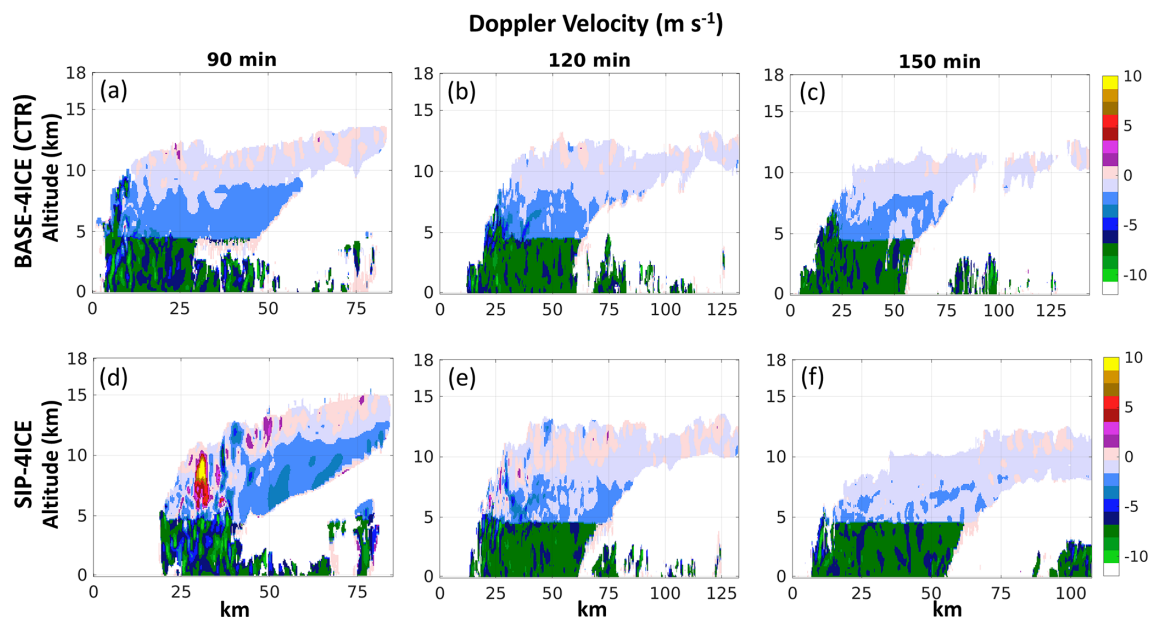
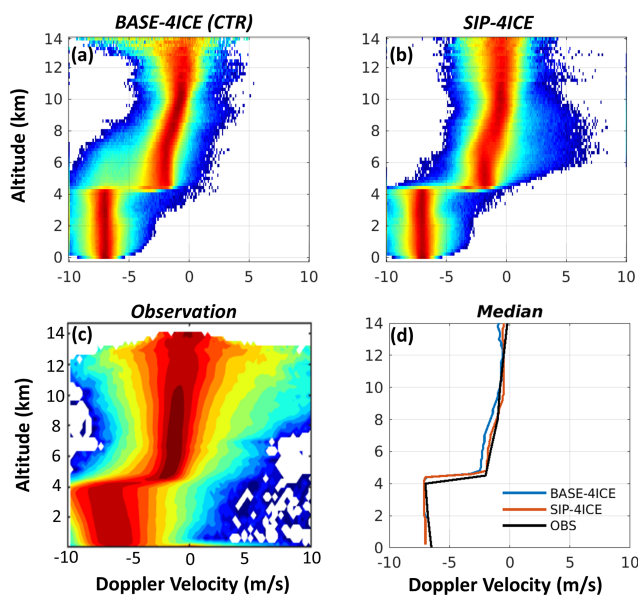**Figure 15.** Simulated Doppler speed for the cross sections indicated by the black lines in Fig. 10.

Figure 16. Same for Fig. 12 but for the Doppler velocity.

6.1 SIP production at different altitudes

Figure 17 shows the active SIP areas and rates at different altitudes for the simulated MCS. Similar to Hu et al. (2021), the values of w are used to distinguish three different situations: (1) SIP within updrafts (marked by red lines, $w > 3\,\mathrm{m\,s^{-1}}$), (2) SIP within downdrafts (marked by yellow lines, $w < 3\,\mathrm{m\,s^{-1}}$), and (3) SIP with moderate vertical wind velocities (marked by blue lines, $-3\,\mathrm{m\,s^{-1}} \leq w \leq 3\,\mathrm{m\,s^{-1}}$).

For the employed SIP parameterizations, FFD is active in the range of altitudes $5 < H < 8.8\,\mathrm{km}$ (Fig. 17e), whereas HM occurs in a narrower range of $5.2 < H < 6.8\,\mathrm{km}$ (Fig. 17a). The range of the SIP activation altitudes is primarily determined by the temperature ranges of the FFD and HM processes (Sect. 2) as well as the temperature of the cloud base. The vertical velocity has a lesser effect on the SIP activation altitudes, and it may displace the upper and lower boundaries of the SIP regions within approximately $\pm 200\,\mathrm{m}$. Within these altitude ranges, SIP is mostly found in the area with moderate vertical wind velocities, followed by the area within updrafts, and occurs less in downdrafts for both the HM and FFD processes (Fig. 17a, e). The active SIP areas of FFD are usually smaller than those of the HM process in the range of altitudes $5.5 < H < 6.2\,\mathrm{km}$ for all three situations. To activate the FFD process, the employed parameterization requires the presence of large raindrops ($100\,\mu\mathrm{m} < D < 3500\,\mu\mathrm{m}$) as well as the presence of small ice particles ($D < 100\,\mu\mathrm{m}$). This condition likely restricts the FFD process to a smaller area than that of the HM process.

The vertical wind speed has a significant impact on the rate of SIP. Figure 17g shows the average SIP rates ($\mathrm{m^{-3}\,s^{-1}}$) within the active FFD areas shown in Fig. 17e. For most altitudes, the rate of FFD increases with an increase in w, and it is at least 1 order of magnitude higher in updrafts than in downdrafts. This is related to the lower number of precipitation-sized drops in downdrafts compared with updrafts.

Another factor is related to the effect of w on the residence time of drops within the range of the SIP activation altitude ΔH. For a drop with a terminal fall veloc-
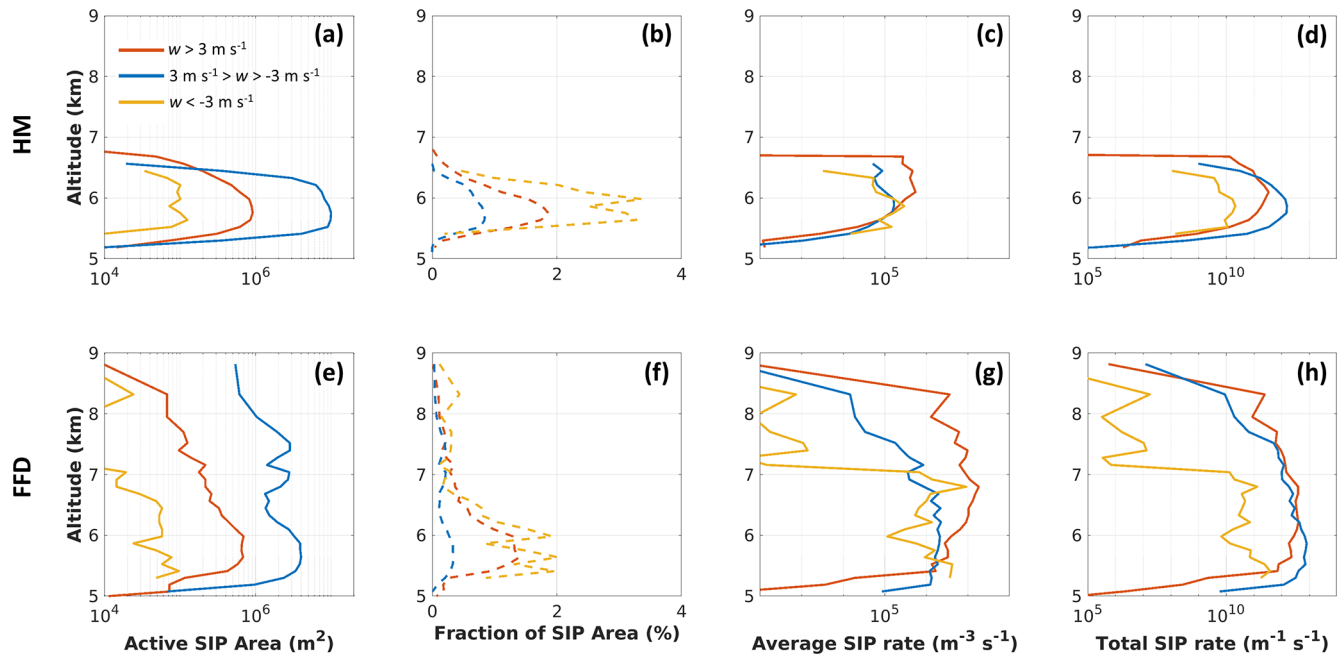
Figure 17. Panel **(a)** presents the area (in m^2) with an active HM process; panel **(b)** presents the fraction of area with an active HM process; panel **(c)** displays the average rate of SIP by the HM process within the active area shown in panel **(a)**; and panel **(d)** shows the total SIP rate, which is the product of panels **(a)** and **(c)**. Panels **(e)**–**(h)** are the same as panels **(a)**–**(d)** but for the FFD process. Red lines (updrafts) denote SIP with $w > 3\,\mathrm{m\,s^{-1}}$, blue lines (outside of updrafts/downdrafts) denote SIP with w between -3 and $3\,\mathrm{m\,s^{-1}}$, and yellow lines (downdrafts) denote SIP with $w < -3\,\mathrm{m\,s^{-1}}$. All results are temporal averages between 90 and 120 min.

ity $V_{\mathrm{fall}}(D)$, the residence time can be assessed as follows: $\tau = \mathrm{abs}\left(\Delta H / (V_{\mathrm{fall}}(D) - w)\right)$. Depending on the sign of $(V_{\mathrm{fall}}(D)w)$, the drop will be moved upward through ΔH or downward. For the extreme situation when $V_{\mathrm{fall}}(D) = w$, the drop is suspended in an updraft indefinitely, and it can freeze and generate secondary ice or mechanically interact with other cloud particles, thereby changing its fall velocity.

The rate of the HM process (Fig. 17c) is higher in updrafts above 6.0 km where the riming process is active. At altitudes below 6.0 km, the rates are similar in updrafts, downdrafts, and areas with moderate vertical velocities ($-3\,\mathrm{m\,s^{-1}} \leq w \leq 3\,\mathrm{m\,s^{-1}}$). Figure 17d shows the total SIP rate ($\mathrm{m^{-1}\,s^{-1}}$) from the HM process; this is the product of the surface of the area with an active HM process and the mean SIP rate from the HM process, as shown in Fig. 17a and c. The total SIP rate shows how many ice particles are produced by SIP horizontally across the domain per 1 m of vertical layer per second. The total SIP rate from the FFD process is shown in Fig. 17h. Below an altitude of 6.3 km, both the HM and FFD processes in the areas with moderate vertical wind velocities show the highest total SIP rate, followed by the area within updrafts. The lowest total rates are found in downdrafts. The larger active SIP areas associated with moderate vertical wind velocities (Fig. 17a, e) contribute significantly to the high total SIP rates across the domain. At altitudes above 6.3 km, updraft regions contribute more to the total SIP rates. This is due to the high average rates in updrafts

(Fig. 17c, g), as the corresponding SIP areas are smaller than those with moderate vertical velocities.

The results obtained show that the vertical extent ΔH of FFD is deeper and its rate is higher than those of HM. This finding leads to the conclusion that the overall contribution of FFD to the production of the secondary ice in tropical MCSs is significantly higher than that of HM in the simulations in this study.

6.2 The role of SIP in initiating of secondary convection

The freezing of rain into ice and the vapour growth of ice splinters generate latent heating which should enhance the existing convection. This may explain the increase in w_{max} above 6 km in Figs. 6c and 7c in SIP-4ICE compared with CTR. As explained in the previous subsection, below 6.3 km altitude, both FFD and HM are more active outside of the major updrafts originating below the melting layer. High activity of the FFD and HM processes might eventually initiate new updrafts in stratiform regions inside MCSs above the melting areas.

A Lagrangian trajectory analysis was used to trace the cloud parcels affected by SIP. For this analysis, 1152 air parcels were selected with active SIP at an altitude of 5.6 km from the SIP-4ICE simulation between 90 and 150 min. Each selected parcel was traced backward ($t < 0\,\mathrm{min}$) and forward ($t > 0\,\mathrm{min}$) for 15 min ($\Delta t = 30\,\mathrm{min}$). These parcels were

then classified into two different groups. The first group included the parcels that had altitudes within $5 < H < 6$ km at $t = -15$ min and ended their trajectories at $H > 6.5$ km at $t = 15$ min. The second group included parcels with the same initial altitudes as the first group at $t = 0$ min; however, the altitude of their trajectories remained at $H < 6$ km at the end of forward tracing ($t = 15$ min). The total number of parcels of the first category was 47 and that of the second category was 1105.

Figure 18 shows the time history of mean values of environmental and microphysical parameters of the parcels for the two categories. Most parcels that underwent SIP processes between −5 and 5 min were located at the same altitude of 5.6 km at $t = 0$ min. These parcels started to rise from $t = -3$ min, and they eventually reached 7.5 km at $t = 15$ min (Fig. 18c). On the other hand, the other group of parcels did not rise throughout the 30 min analysis period (hereafter named "non-rising parcels"). The mean altitude of these parcels decreased by about 700 m (Fig. 18c).

Figure 18e shows that the rising parcels had an initial positive vertical speed from $t = -3$ to −1 min. However, their potential temperature differences with respect to the environmental values at the same altitudes ($\Delta\theta$) were generally negative for $t < -1$ min and decreased slightly from $t = -3$ to −1 min (Fig. 18g). Thus, these parcels were not gaining positive buoyancy at this stage. However, the $\Delta\theta$ of the rising parcels started to increase quickly between $t = 0$ min and 2 min, becoming positive and reaching a difference of nearly +1 K between $t = 3$ and 8 min (Fig. 18g). Figure 18i and j also show very high SIP rates for the rising parcels from the FFD process during this time period. For the non-rising parcels, there was an increase in $\Delta\theta$ during the same period but at a much slower rate due to a smaller SIP tendency (Fig. 18i, j). The $\Delta\theta$ remained negative during the whole analysis period; therefore, these parcels were convectively stable.

The main reason for the high SIP rate between $t = 0$ and 2 min for the rising parcels is that there was a substantial amount of large rain drops available for activating the FFD process (Fig. 18f, h). The rain mean-mass diameter at $t = 0$ min was large (560 μm). The RWC was also large (0.36 g m^{-3}). The rain mean-mass diameter for the non-rising parcels (502 μm) was slightly smaller than that of rising parcels at $t = 0$ min. However, the corresponding RWC was quite low (0.02 g m^{-3}). With a large RWC and rain mean-mass diameter, the rising parcels had a high SIP potential, which eventually led to greater N_i, vapour growth, and increased latent heating and buoyancy, thereby enhancing secondary convection.

As mentioned in Sect. 6.1, the FFD process plays a dominant role in SIP compared with the HM process in the simulations of this study. This agrees with what we found in Fig. 18i and j. The sudden increase in the $\Delta\theta$ with respect to the environment is more likely linked to the high SIP rate from FFD.

Therefore, SIP, in particular FFD, may play a role in the initiation of new updrafts above the melting layer.

Figure 19 shows an example of a rising air parcel. The black line represents the parcel trajectory from $t = -15$ to 15 min. From $t = -15$ to 0 min, the air parcel had no significant change in altitude. Near $t = 0$ min, the air parcel was close to an existing updraft (Fig. 19a, red surface) and was in an area where there was rainwater (Fig. 19b, red surface). Shortly after $t = 0$ min, the air parcel started to rise. The supply of rainwater resulted in an enhanced SIP and led to a higher rate of latent heating and rapid increase in buoyancy.

7 Impact of ice aggregation

In addition to SIP, which clearly has significant effects on N_i, the formation of high IWC, radar reflectivity, and vertical wind velocity, the aggregation of ice particles also plays an important role in determining the microstructure. Aggregation results in a decrease in N_i and an increase in radar reflectivity and particle fall velocity. The rate of aggregation is characterized by the ice–ice collection efficiency (e_{ii}). In the framework of this study, the following parameterization of the ice–ice collection efficiency has been employed (Cotton et al., 1986):

$$e_{ii} = \min(10^{0.035(T-237.16)-0.7}, 0.2), \tag{4}$$

where T is the temperature in kelvin.

There is a diversity of parameterizations of e_{ii} employed in models (Khain and Pinsky, 2018), which may vary by up to 3 orders of magnitude. In this study, the mid-range e_{ii} in Eq. (4) is used as the default parameterization. However, the uncertainty in e_{ii} raises a question about the impact of the ice aggregation parameterization on the N_i and high IWC formation.

To explore the effect of the ice aggregation rate on the high IWC formation, a sensitivity test (SIP-COL) was performed with another e_{ii} parameterization, i.e.,

$$e_{ii} = \begin{cases} 0.1 & \text{for } T < -20\,°\text{C}; \\ 0.06T + 1.3 & \text{for } -20 < T < -5\,°\text{C}; \\ 1 & \text{for } -5 < T < 0\,°\text{C}. \end{cases} \tag{5}$$

As seen from Eq. (5), the new e_{ii} varied linearly from 0.1 to 1.0 within the $-20° < T < -5\,°$C temperature range: for $T < -20\,°$C, $e_{ii} = 0.1$; for $-5\,°$C, $< T < 0\,°$C $e_{ii} = 1.0$. For all temperatures, e_{ii} in Eq. (5) is much higher than that in Eq. (4). We want to use this high e_{ii} parameterization to show the significant impact of e_{ii} on the simulation results.

Comparisons of the distributions of N_i for two SIP simulations with varying e_{ii} and the observations are shown in Fig. 20. For the altitudes between 6 and 7 km, using the new parameterization of aggregation (given by Eq. 5) (SIP-COL) results in a decrease in the modal value of $F(N_i)$ by 2 orders of magnitude compared with using that described by Eq. (4) (SIP-4ICE). At higher altitudes between 10 and 11 km, the
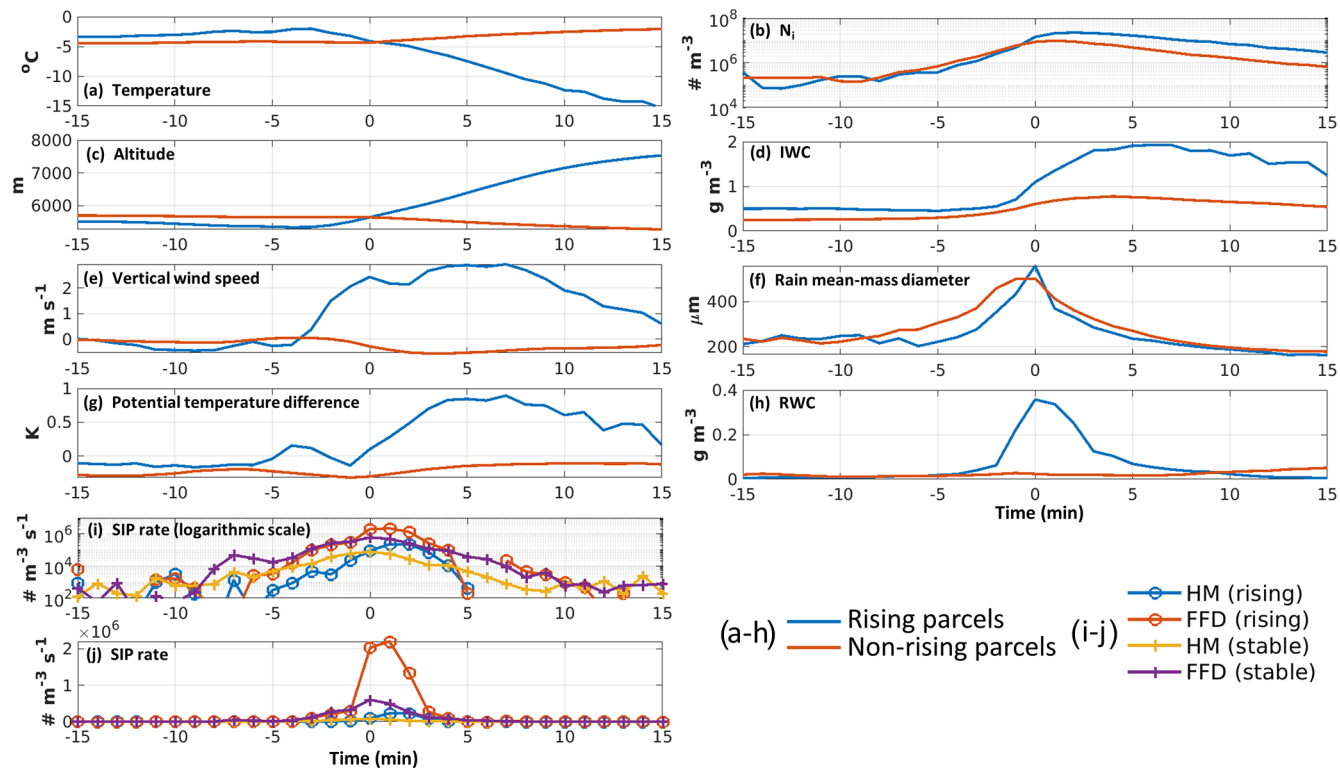
Figure 18. Trajectory tracing of different variables for the rising parcels (blue lines in **a–h**) and the non-rising parcels (red lines in **a–h**) for **(a)** temperature, **(b)** N_i, **(c)** altitude, **(d)** IWC, **(e)** vertical wind speed, **(f)** rain mean-mass diameter, **(g)** $\Delta\theta$, **(h)** RWC, **(i)** SIP tendency in logarithmic scale, and **(j)** SIP tendency in regular scale.
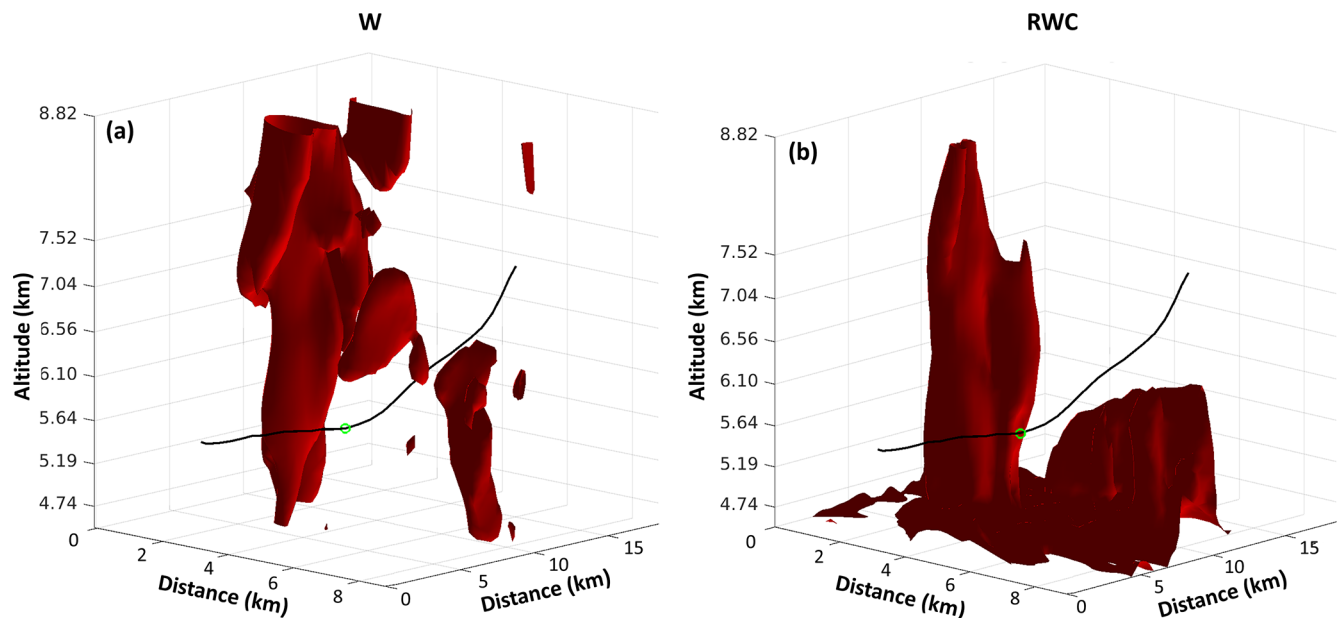

Figure 19. The trajectory of a specific air parcel (black line), and the location of the parcel at $t = 0$ min (green circle). The red surfaces in panel **(a)** show the area with w larger than $3\,\mathrm{m\,s^{-1}}$ at the moment of $t = 0$ min, and red surfaces in panel **(b)** show the area with RWC larger than $0.05\,\mathrm{g\,m^{-3}}$ at the moment of $t = 0$ min.
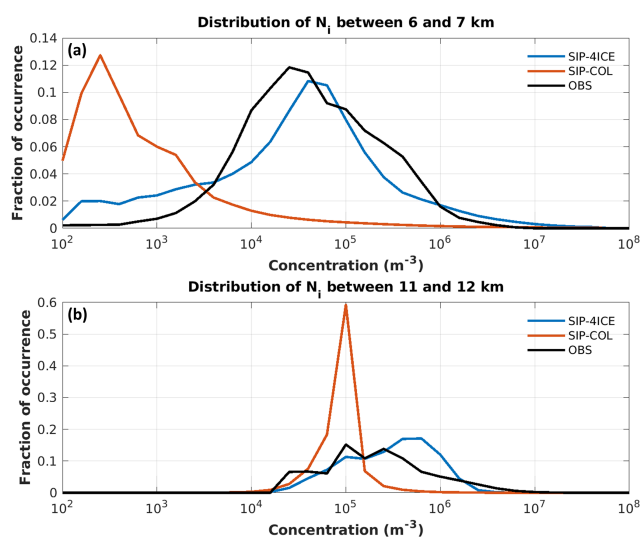
Figure 20. Similar to Fig. 8 but for SIP-4ICE and SIP-COL.
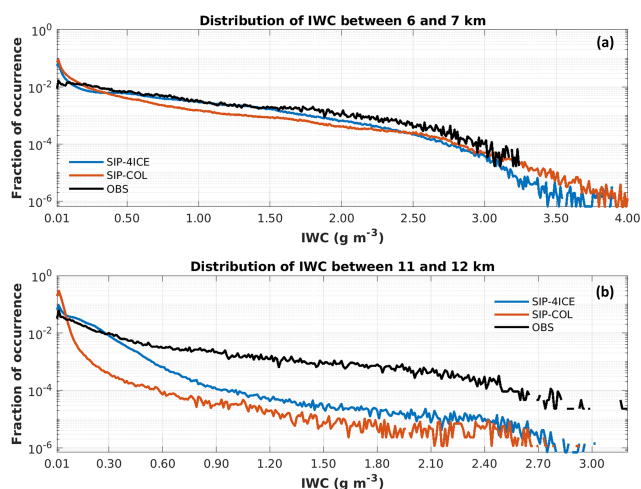
Figure 21. Similar to Fig. 9 but for SIP-4ICE and SIP-COL.

SIP-COL run produces ~ 5 times higher $F(N_i)$ at N_i values of $10^5\,\mathrm{m}^{-3}$ and lower $F(N_i)$ by 1–2 orders of magnitude for $N_i > 4 \times 10^5\,\mathrm{m}^{-3}$ compared with those of SIP-4ICE.

Figure 21 shows similar results to Fig. 20 but for the distribution of ice mass. Between 6 and 7 km, applying the linear approach for e_{ii} from Eq. (5) to the SIP-4ICE simulation (SIP-COL), the $F(\mathrm{IWC})$ between 0.4 and 2.4 g m^{-3} is slightly reduced by up to 50 %. However, the $F(\mathrm{IWC})$ for an extreme situation with an IWC value larger than 2.5 g m^{-3} is somehow slightly enhanced.

For altitudes between 11 and 12 km, the SIP-COL experiment produces a lower $F(\mathrm{IWC})$, by up to ~ 1 order of magnitude for most IWC values (> 0.16 g m^{-3}), than the SIP-4ICE simulation. Although the estimation of $F(\mathrm{IWC})$ by SIP-COL between 6 and 7 km is relatively close to that of SIP-4ICE, SIP-COL produces much lower $F(\mathrm{IWC})$ at higher altitudes,

between 10 and 11 km, than the SIP-4ICE simulation. This indicates that the N_i values at lower altitudes play an important role in determining the IWC at upper altitudes.

8 Conclusion

The impacts of SIP on the microphysics and dynamics of deep convection have been examined using quasi-idealized near-cloud-resolving simulations of a tropical MCS based on storm observations during the HAIC-HIWC field campaign. GEM model simulations using the P3 microphysics scheme were conducted using a 250 m horizontal grid spacing and horizontally homogeneous atmospheric initial conditions, with updraft nudging to initiate convection. It was established through sensitivity tests that a minimum of three ice categories in P3 are necessary to examine SIP in detail; four categories were used for most of the simulations. P3 was modified to include rime splintering (HM) and fragmentation of freezing drops (FFD), which have been the most closely examined SIP mechanisms in laboratory studies. The parameterizations of the HM and FFD processes used were based on the information available from previously published results.

In the control configuration with no SIP processes at altitudes of 6 to 7 km, the simulated ice number concentrations were about 2 orders of magnitude lower than the values obtained from in situ measurements. The simulated frequency of encountering high-IWC conditions is about 1/2 to 1/500 of the observed frequency between IWC values of 1 and 2 g m^{-3}. With the SIP mechanisms activated, the model results for these fields were dramatically improved compared with the observations. The Doppler velocities above the melting layer were also notably closer to the measured values, indicating improved ice fall speeds in the simulations with SIP active. SIP was responsible for an increase in the ice concentrations of up to 3 orders of magnitude at altitudes of 6 to 7 km. As a result, the total ice mass was distributed over a much larger number of particles; thus, the mean particle size was smaller with a lower fall speed. Consequently, ice was more easily transported to higher altitudes, ultimately resulting in sustained cloud regions with high IWC.

Analysis conducted in this study led to the following general conclusions for the high-resolution NWP simulations:

1. SIP processes play a critical role in the formation and maintenance of high IWC with low reflectivity at upper levels in MCSs.

2. SIP enhances secondary convection above the melting layer due to an increase in buoyancy caused by greater latent heat release during vapour deposition on numerous secondary ice particles. Enhanced secondary convection may, in turn, extend the longevity of MCSs and regions with high IWC.
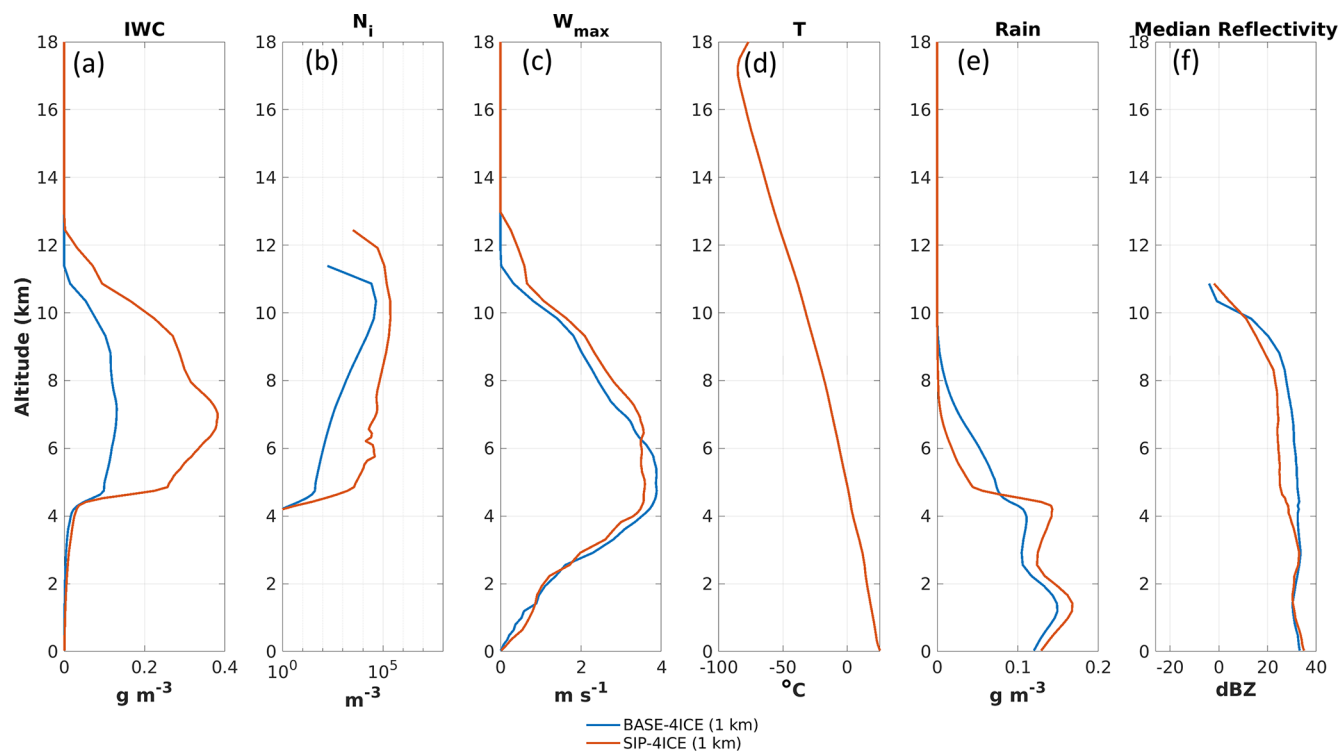
Figure 22. Similar to Fig. 6 but for simulation at a 1 km horizontal grid spacing.

3. Aggregation of ice particles results in a decrease in the ice number concentration and IWC at upper levels but is very sensitive to details of the parameterization of this process, in particular the collection efficiency, which remains uncertain.

In order to minimize errors in the interpretation of the results due to unresolved convective updrafts, the simulations conducted in this study were all done with a horizontal grid spacing of 250 m. This is a much higher resolution than that of current operational NWP models; however, tests with a 1 km grid spacing (Fig. 22) indicated that the impacts of including SIP are very similar to those at a 250 m grid spacing, where 1 km is close to the grid spacing of several current operational and experimental NWP systems. Furthermore, the P3 microphysics scheme is already used operationally in the Canadian 2.5 km system (Milbrandt et al., 2015). Therefore, the conclusions regarding the importance of including SIP processes in models are not limited to numerical modelling in research mode but also have important implications for current and/or upcoming operational NWP, in particular for systems that provide numerical guidance for civil aviation operating at cruising altitudes between 10 and 14 km.

Finally, although the simulations conducted with the activated SIP process clearly resulted in improved results compared with the observations, this is not a basis for concluding that the HM and FFD parameterizations used are accurate representations of these physical processes. While the formulations were based on either laboratory experiments or combined modelling and in situ observational study, they are still largely ad hoc. This study further highlights the importance of these processes in deep convection and the need to include them in some fashion in numerical models. However, accurate parameterizations that capture the underlying physics of these mechanisms, not just their bulk effects, continue to be topics of research.

Author contributions. ZQ, AK, and JAM conceptualized the research goals and aims. ZQ, JAM, and AK designed the experiments with the support from YH, GMM, and HM. ZQ performed the simulations and analysis with the help from AK, JAM, IH, MW, and CN. ZQ prepared the manuscript with contributions from all co-authors.

References

Ackerman, A. S., Fridlind, A. M., Grandin, A., Dezitter, F., Weber, M., Strapp, J. W., and Korolev, A. V.: High ice water content at low radar reflectivity near deep convection – Part 2: Evaluation of microphysical pathways in updraft parcel simulations, Atmos. Chem. Phys., 15, 11729–11751, https://doi.org/10.5194/acp-15-11729-2015, 2015.

Baumgardner, D., Jonsson, H. H., Dawson, W., O'Connor, D. P., and Newton, R.: The Cloud, Aerosol and Precipitation Spectrometer: A New Instrument for Cloud Investigations, Atmos. Res., 59–60, 251–264, https://doi.org/10.1016/S0169-8095(01)00119-3, 2001.

Baumgardner, D., Abel, S. J., Axisa, D., Cotton, R., Crosier, J., Field, P., Gurganus, C., Heymsfield, A., Korolev, A., Krämer, M., Lawson, P., McFarquhar, G., Ulanowski, Z., and Um, J.: Cloud Ice Properties: In Situ Measurement Challenges, Meteor. Mon., 58, 9.1–9.23, https://doi.org/10.1175/AMSMONOGRAPHS-D-16-0011.1, 2017.

Bryan, G. H., Wyngaard, J. C., and Fritsch, J. M.: Resolution requirements for the simulation of deep moist convection, Mon. Weather Rev., 131, 2394–2416, https://doi.org/10.1175/1520-0493(2003)131<2394:RRFTSO>2.0.CO;2, 2003.

Cantrell, W. and Heymsfield, A.: Production of ice in tropospheric clouds: A review, B. Am. Meteorol. Soc., 86, 795–808, https://doi.org/10.1175/BAMS-86-6-795, 2005.

Cholette, M., Morrison, H., Milbrandt, J. A., and Thériault, J. M.: Parameterization of the bulk liquid fraction on mixed-phase particles in the Predicted Particle Properties (P3) scheme: Description and idealized simulations, J. Atmos. Sci., 76, 561–582, https://doi.org/10.1175/jas-d-18-0278.1, 2019.

Côté, J., Gravel, S., Méthot, A., Patoine, A., Roch, M., and Staniforth, A.: The operational CMC–MRB global environmental multiscale (GEM) model. Part I: Design considerations and formulation, Mon. Weather.

Rev., 126, 1373–1395, https://doi.org/10.1175/1520-0493(1998)126<1373:TOCMGE>2.0.CO;2, 1998.

Cotton, W. R., Tripoli, G. J., Rauber, R. M., and Mulvihill, E. A.: Numerical simulation of the effects of varying ice crystal nucleation rates and aggregation processes on orographic snowfall, J. Clim. Appl. Meteorol., 25, 1658–1680, 1986.

Davison, C. R., MacLeod, J. D., Strapp, J. W., and Buttsworth, D. R.: Isokinetic Total Water Content Probe in a Naturally Aspirating Configuration: Initial Aerodynamic Design and Testing, 2008, AIAA Paper 2008-0435, 46th AIAA Aerospace Sciences Meeting and Exhibit, 10 January 2008, Reno, Nevada. 2008.

Dedekind, Z., Lauber, A., Ferrachat, S., and Lohmann, U.: Sensitivity of precipitation formation to secondary ice production in winter orographic mixed-phase clouds, Atmos. Chem. Phys., 21, 15115–15134, https://doi.org/10.5194/acp-21-15115-2021, 2021.

Dye, J. E. and Hobbs P. V.: The influence of environmental parameters on the freezing and fragmentation of suspended water drops, J. Atmos. Sci., 25, 82–96, https://doi.org/10.1175/1520-0469(1968)025<0082:TIOEPO>2.0.CO;2, 1968.

Environment and Climate Change Canada: The Global Environmental Multiscale Model (GEM) (version 5.1.0-rc3), GitHub [code], https://github.com/ECCC-ASTD-MRD/gem/tree/5.1.0-rc3 (last access 12 September 2022), 2020.

Ferrier, B. S.: A two-moment multiple-phase four-class bulk ice scheme. Part I: Description, J. Atmos. Sci., 51, 249–280, 1994.

Ferrier, B. S., Tau, W.-K., and Simpson, J.: A two-moment multiple phase four-class bulk ice scheme. Part II: Simulations of convective storms in different large-scale environments and comparisons with other bulk parameterizations, J. Atmos. Sci., 52, 1001–1033, 1995.

Field, P. R., Heymsfield, A. J., and Bansemer, A.: Shattering and Particle Inter-arrival Times Measured by Optical Array Probes in Ice Clouds, J. Atmos. Ocean. Tech., 23, 1357–1370, 2006.

Field, P. R., Lawson, R. P., Brown, P. R. A., Lloyd, G., Westbrook, C., Moisseev, D., Miltenberger, A., Nenes, A., Blyth, A., Choularton, T., Connolly, P., Buehl, J., Crosier, J., Cui, Z., Dearden, C., DeMott, P., Flossmann, A., Heymsfield, A., Huang, Y., Kalesse, H., Kanji, Z. A., Korolev, A., Kirchgaessner, A., Lasher-Trapp, S., Leisner, T., McFarquhar, G., Phillips, V., Stith, J., and Sullivan, S.: Secondary Ice Production: Current State of the Science and Recommendations for the Future, Meteor. Mon., 58, 7.1–7.20, https://doi.org/10.1175/amsmonographs-d-16-0014.1, 2017.

Franklin, C. N., Protat, A., Leroy, D., and Fontaine, E.: Controls on phase composition and ice water content in a convection-permitting model simulation of a tropical mesoscale convective system, Atmos. Chem. Phys., 16, 8767–8789, https://doi.org/10.5194/acp-16-8767-2016, 2016.

Fridlind, A. M., Ackerman, A. S., Grandin, A., Dezitter, F., Weber, M., Strapp, J. W., Korolev, A. V., and Williams, C. R.: High ice water content at low radar reflectivity near deep convection – Part 1: Consistency of in situ and remote-sensing observations with stratiform rain column simulations, Atmos. Chem. Phys., 15, 11713–11728, https://doi.org/10.5194/acp-15-11713-2015, 2015.

Fu, S., Deng, X., Shupe, M. D., and Xue, H.: A modelling study of the continuous ice formation in an autumn-

nal Arctic mixed-phase cloud case, Atmos. Res., 228, 77–85, https://doi.org/10.1016/j.atmosres.2019.05.021, 2019.

Gayet, J.-F., Mioche, G., Bugliaro, L., Protat, A., Minikin, A., Wirth, M., Dörnbrack, A., Shcherbakov, V., Mayer, B., Garnier, A., and Gourbeyre, C.: On the observation of unusual high concentration of small chain-like aggregate ice crystals and large ice water contents near the top of a deep convective cloud during the CIRCLE-2 experiment, Atmos. Chem. Phys., 12, 727–744, https://doi.org/10.5194/acp-12-727-2012, 2012.

Girard, C., Desgagné, M., McTaggart-Cowan, R., Côté, J., Charron, M., Gravel, S., Lee, V., Patoine, A., Qaddouri, A., Roch, M., Spacek, L., Tanguay, M., Vaillancourt, P. A., and Zadra, A.: Staggered vertical discretization of the Canadian environmental multiscale (GEM) model using a coordinate of the log-hydrostatic-pressure type, Mon. Weather Rev., 142, 1183–1196, https://doi.org/10.1175/MWR-D-13-00255.1, 2014.

Hallett, J. and Mossop, S.: Production of secondary ice particles during the riming process, Nature, 249, 26–28, https://doi.org/10.1038/249026a0, 1974.

Hallgren, R. E. and Hosler, C. L.: Preliminary results on the aggregation of ice crystals, in: Physics of Precipitation: Proceedings of the Cloud Physics Conference, Woods Hole, Massachusetts, 3–5 June 1959, American Geophysical Union, 257–263, https://doi.org/10.1029/GM005p0257, 1960.

Hawker, R. E., Miltenberger, A. K., Johnson, J. S., Wilkinson, J. M., Hill, A. A., Shipway, B. J., Field, P. R., Murray, B. J., and Carslaw, K. S.: Model emulation to understand the joint effects of ice-nucleating particles and secondary ice production on deep convective anvil cirrus, Atmos. Chem. Phys., 21, 17315–17343, https://doi.org/10.5194/acp-21-17315-2021, 2021.

Heymsfield, A. J. and Parrish, J. L.: Techniques employed in the processing of particle size spectra and state parameter data obtained with the T-28 aircraft platform (No. NCAR/TN-137+IA), University Corporation for Atmospheric Research, https://https://doi.org/10.5065/D6639MPN, 1979.

Heymsfield, A. J. and Palmer, A.: Relationship for deriving thunderstorm anvil ice mass for CCOPE storm weather estimates, J. Clim. Appl. Meteorol., 25, 691–702, https://doi.org/10.1175/1520-0450(1986)025<0691:RFDTAI>2.0.CO;2, 1986.

Hoarau, T., Pinty, J.-P., and Barthe, C.: A representation of the collisional ice break-up process in the two-moment microphysics LIMA v1.0 scheme of Meso-NH, Geosci. Model Dev., 11, 4269–4289, https://doi.org/10.5194/gmd-11-4269-2018, 2018.

Hobbs, P. V. and Rangno, A. L.: Ice particle concentrations in clouds, J. Atmos. Sci., 42, 2523–2549, https://doi.org/10.1175/1520-0469(1985)042<2523:IPCIC>2.0.CO;2, 1985.

Hu, Y., McFarquhar, G. M., Wu, W., Huang, Y., Schwarzenboeck, A., Protat, A., Korolev, A., Rauber, R. M., and Wang, H.: Dependence of Ice Microphysical Properties On Environmental Parameters: Results from HAIC-HIWC Cayenne Field Campaign, J. Atmos. Sci., 78, 2957–2981, https://doi.org/10.1175/JAS-D-21-0015.1, 2021.

Huang, Y., Wu, W., McFarquhar, G. M., Wang, X., Morrison, H., Ryzhkov, A., Hu, Y., Wolde, M., Nguyen, C., Schwarzenboeck, A., Milbrandt, J., Korolev, A. V., and Heckman, I.: Microphysical processes producing high ice water contents (HIWCs) in tropical convective clouds during the HAIC-HIWC field campaign:

evaluation of simulations using bulk microphysical schemes, Atmos. Chem. Phys., 21, 6919–6944, https://doi.org/10.5194/acp-21-6919-2021, 2021.

Huang, Y., Wu, W., McFarquhar, G. M., Xue, M., Morrison, H., Milbrandt, J., Korolev, A. V., Hu, Y., Qu, Z., Wolde, M., Nguyen, C., Schwarzenboeck, A., and Heckman, I.: Microphysical processes producing high ice water contents (HIWCs) in tropical convective clouds during the HAIC-HIWC field campaign: dominant role of secondary ice production, Atmos. Chem. Phys., 22, 2365–2384, https://doi.org/10.5194/acp-22-2365-2022, 2022.

James, R. L., Phillips, V. T. J., and Connolly, P. J.: Secondary ice production during the break-up of freezing water drops on impact with ice particles, Atmos. Chem. Phys., 21, 18519–18530, https://doi.org/10.5194/acp-21-18519-2021, 2021.

Kanji, Z. A., Ladino, L. A., Wex, H., Boose, Y., Burkert-Kohn, M., Cziczo, D. J., and Krämer, M.: Overview of ice nucleating particles, Meteor. Mon., 58, 1.1–1.33, https://doi.org/10.1175/AMSMONOGRAPHS-D-16-0006.1, 2017.

Khain, A. P. and Pinsky, M.: Physical processes in clouds and cloud modeling. Cambridge University Press, UK and New York, NY, USA, 626 pp., https://doi.org/10.1017/9781139049481, 2018.

Keinert, A., Spannagel, D., Leisner, T., and Kiselev, A.: Secondary ice production upon freezing of freely falling drizzle droplets, J. Atmos. Sci., 77, 2959–2967, https://doi.org/10.1175/JAS-D-20-0081.1, 2020.

Keppas, S. C., Crosier, J., Choularton, T. W., and Bower, K. N.: Ice lollies: An ice particle generated in supercooled conveyor belts, Geophys. Res. Lett., 44, 5222–5230, https://doi.org/10.1002/2017GL073441, 2017.

Kleinheins, J., Kiselev, A., Keinert, A., Kind, M., and Leisner, T.: Thermal imaging of freezing drizzle droplets: pressure release events as a source of secondary ice particles, J. Atmos. Sci., 78, 1703–1713, https://doi.org/10.1175/jas-d-20-0323.1, 2021.

Knapp, K. R. and Wilkins, S. L.: Gridded Satellite (GridSat) GOES and CONUS data, Earth Syst. Sci. Data, 10, 1417–1425, https://doi.org/10.5194/essd-10-1417-2018, 2018.

Koenig, L. R.: The Glaciating Behaviour of Small Cumulonimbus Clouds, J. Atmos. Sci., 20, 29–47, https://doi.org/10.1175/1520-0469(1963)020<0029:TGBOSC>2.0.CO;2, 1963.

Koenig, L. R.: Drop freezing through drop breakup. J. Atmos. Sci., 22, 448–451, https://doi.org/10.1175/1520-0469(1965)022<0448:DFTDB>2.0.CO;2, 1965.

Korolev, A. and Field, P. R.: Assessment of the performance of the inter-arrival time algorithm to identify ice shattering artifacts in cloud particle probe measurements, Atmos. Meas. Tech., 8, 761–777, https://doi.org/10.5194/amt-8-761-2015, 2015.

Korolev, A. and Leisner, T.: Review of experimental studies of secondary ice production, Atmos. Chem. Phys., 20, 11767–11797, https://doi.org/10.5194/acp-20-11767-2020, 2020.

Korolev, A. and Sussman, B.: A Technique for Habit Classification of Cloud Particles, J. Atmos. Ocean. Tech., 17, 1048–1057, https://doi.org/10.1175/1520-0426(2000)017<1048:ATFHCO>2.0.CO;2, 2000.

Korolev, A., Heckman, I., Wolde, M., Ackerman, A. S., Fridlind, A. M., Ladino, L. A., Lawson, R. P., Milbrandt, J., and Williams, E.: A new look at the environmental conditions favorable to secondary ice production, Atmos. Chem. Phys., 20, 1391–1429, https://doi.org/10.5194/acp-20-1391-2020, 2020.

Ladino, L. A., Korolev, A., Heckman, I., Wolde, M., Fridlind, A. M., and Ackerman, A. S.: On the role of ice-nucleating aerosol in the formation of ice particles in tropical mesoscale convective systems, Geophys. Res. Lett., 44, 1574–1582, https://doi.org/10.1002/2016GL072455, 2017.

Lance, S., Brock, C. A., Rogers, D., and Gordon, J. A.: Water droplet calibration of the Cloud Droplet Probe (CDP) and in-flight performance in liquid, ice and mixed-phase clouds during ARCPAC, Atmos. Meas. Tech., 3, 1683–1706, https://doi.org/10.5194/amt-3-1683-2010, 2010.

Lasher-Trapp, S., Leon, D. C., DeMott, P. J., Villanueva-Birriel, C. M., Johnson, A. V., Moser, D. H., Tully, C. S., and Wu, W.: A Multisensor Investigation of Rime Splintering in Tropical Maritime Cumuli, J. Atmos. Sci., 73, 2547–2564, https://doi.org/10.1175/JAS-D-15-0285.1, 2016.

Lawson, R. P., Angus, L. J., and Heymsfield, A. J.: Cloud Particle Measurements in Thunderstorm Anvils and Possible Threat to Aviation, J. Aircraft, 35, 113–121, 1998.

Lawson, R. P., O'Connor, D., Zmarzly, P., Weaver, K., Baker, B., Mo, Q., and Jonsson, H.: The 2D-S (stereo) probe: Design and preliminary tests of a new airborne, high speed, high-resolution particle imaging probe, J. Atmos. Ocean. Tech., 23, 1462–1477, https://doi.org/10.1175/JTECH1927.1, 2006.

Lawson, R. P., Woods, S., and Morrison, H.: The microphysics of ice and precipitation development in tropical cumulus clouds, J. Atmos. Sci., 72, 2429–2445, https://doi.org/10.1175/JAS-D-14-0274.1, 2015.

Lawson, R. P., Gurganus, C., Woods, S., and Bruintjes, R.: Aircraft observations of cumulus microphysics ranging from the tropics to midlatitudes: Implications for a "new" secondary ice process, J. Atmos. Sci., 74, 2899–2920, https://doi.org/10.1175/JAS-D-17-0033.1, 2017.

Lebo, Z. J. and Morrison, H.: Effects of horizontal and vertical grid spacing on mixing in simulated squall lines and implications for convective strength and structure, Mon. Weather Rev., 143, 4355–4375, https://doi.org/10.1175/MWR-D-15-0154.1, 2015.

Leroy, D., Fontaine, E., Schwarzenboeck, A., Strapp, J. W., Korolev, A., McFarquhar, G., Dupuy, R., Gourbeyre, C., Lilie, L., Protat, A., Delanoe, J., Dezitter, F., and Grandin, A.: Ice crystal sizes in high ice water content clouds. Part II: Statistics of mass diameter percentiles in tropical convection observed during the HAIC/HIWC project, J. Atmos. Ocean. Tech., 34, 117–136, https://doi.org/10.1175/JTECH-D-15-0246.1, 2017.

Li, H., Korolev, A., and Moisseev, D.: Supercooled liquid water and secondary ice production in Kelvin–Helmholtz instability as revealed by radar Doppler spectra observations, Atmos. Chem. Phys., 21, 13593–13608, https://doi.org/10.5194/acp-21-13593-2021, 2021.

Lin, Y.-L., Farley, R. D., and Orville, H. D.: Bulk parameterization of the snow field in a cloud model, J. Clim. Appl. Meteorol., 22, 1065–1092, https://doi.org/10.1175/1520-0450(1983)022<1065:bpotsf>2.0.co;2, 1983.

Lloyd, G., Choularton, T. W., Bower, K. N., Gallagher, M. W., Connolly, P. J., Flynn, M., Farrington, R., Crosier, J., Schlenczek, O., Fugal, J., and Henneberger, J.: The origins of ice crystals measured in mixed-phase clouds at the high-alpine site Jungfraujoch, Atmos. Chem. Phys., 15, 12953–12969, https://doi.org/10.5194/acp-15-12953-2015, 2015.

Luke, E. P., Yang, F., Kollias, P., Vogelmann, A. M., and Maahn, M.: New insights into ice multiplication using remote-sensing observations of slightly supercooled mixed-phase clouds in the Arctic, P. Natl. Acad. Sci. USA, 118, e2021387118, https://doi.org/10.1073/pnas.2021387118, 2021.

Mason, J. G. and Grzych, M.: The Challenges Identifying Weather Associated with Jet Engine Ice Crystal Icing, SAE Technical Paper 2011-38-0094, https://doi.org/10.4271/2011-38-0094, 2011.

Mason, J. G., Strapp, J. W., and Chow, P.: The Ice Particle Threat to Engines in Flight, 44th AIAA Aerospace Sciences Meeting and Exhibit, Reno, Nevada, January 9–12, AIAA 2006-206, https://doi.org/10.2514/6.2006-206, 2006.

Mignani, C., Creamean, J. M., Zimmermann, L., Alewell, C., and Conen, F.: New type of evidence for secondary ice formation at around −15 °C in mixed-phase clouds, Atmos. Chem. Phys., 19, 877–886, https://doi.org/10.5194/acp-19-877-2019, 2019.

Milbrandt, J. and Morrison, H.: Parameterization of cloud microphysics based on the prediction of bulk ice particle properties. Part III: Introduction of multiple free categories, J. Atmos. Sci., 73, 975–995, https://doi.org/10.1175/JAS-D-15-0204.1, 2016.

Milbrandt, J. A. and Yau, M. K.: A multi-moment bulk microphysics parameterization. Part I: Analysis of the role of the spectral shape parameter, J. Atmos. Sci., 62, 3051–3064, https://doi.org/10.1175/JAS3534.1, 2005a.

Milbrandt, J. A. and Yau, M. K.: A multi-moment bulk microphysics parameterization. Part II: A proposed three-moment closure and scheme description, J. Atmos. Sci., 62, 3065–3081, https://doi.org/10.1175/JAS3535.1, 2005b.

Milbrandt, J. A., Bélair, S., Faucher, M., Vallée, M., Carrera, M. A., and Glazer, A.: The Pan-Canadian High Resolution (2.5-km) Deterministic Prediction System, Weather Forecast., 31, 1791–1816, https://doi.org/10.1175/WAF-D-16-0035.1, 2016.

Milbrandt, J. A., Morrison, H., Dawson II, D. T., and Paukert, M.: A triple-moment representation of ice in the Predicted Particle Properties (P3) microphysics scheme, J. Atmos. Sci., 78, 439–458, https://doi.org/10.1175/JAS-D-20-0084.1, 2021.

Morrison, H. and Milbrandt, J. A.: Parameterization of cloud microphysics based on the prediction of bulk ice particle properties. Part I: Scheme description and idealized tests, J. Atmos. Sci., 72, 287–311, https://doi.org/10.1175/JAS-D-14-0065.1, 2015.

Murgatroyd, R. and Garrod, M.: Observations of precipitation elements in cumulus clouds, Q. J. Roy. Meteor. Soc., 86, 167–175, https://doi.org/10.1002/qj.49708636805, 1960.

Naylor, J. and Gilmore, M. S.: Convective initiation in an idealized cloud model using an updraft nudging technique, Mon. Weather Rev., 140, 3699–3705, https://doi.org/10.1175/MWR-D-12-00163.1, 2012.

Oraltay, R. G. and Hallett, J.: Evaporation and melting of ice crystals: A laboratory study, Atmos. Res., 24, 169–189, https://doi.org/10.1016/0169-8095(89)90044-6, 1989.

Paukert, m., Fan, J., Rasch, P. J., Morrison, H., Milbrandt, J., Shpund, J., Khain, A.: Three-moment representation of rain in a bulk microphysics model. J. Adv. Model. Earth Sy., 11, 257–277, https://doi.org/10.1029/2018MS001512, 2019.

Phillips, V. T. J., Yano, J. I., Formenton, M., Ilotoviz, E., Kanawade, V., Kudzotsa, I., Sun, J., Bansemer, A., Detwiler, A. G., Khain, A., and Tessendorf, S. A.: Ice multiplication by breakup in ice-ice collisions. Part II: Numerical simulations, J. Atmos. Sci., 74, 2789–2811, https://doi.org/10.1175/JAS-D-16-0223.1, 2017.

Phillips, V. T., Patade, S., Gutierrez, J., and Bansemer, A.: Secondary ice production by fragmentation of freezing drops: Formulation and theory, J. Atmos. Sci., 75, 3031–3070, https://doi.org/10.1175/JAS-D-17-0190.1, 2018.

Prabhakaran, P., Kinney, G., Cantrell, W., Shaw, R. A., and Bodenschatz, E.: High supersaturation in the wake of fallinghydrometeors: Implications for cloud invigoration and ice nucleation, Geophys. Res. Lett., 47, e2020GL088055, https://doi.org/10.1029/2020GL088055, 2020.

Reisner, J., Rasmussen, R. M., and Bruintjes, R. T.: Explicit forecasting of supercooled liquid water in winter storms using the MM5 mesoscale model, Q. J. Roy. Meteor. Soc., 124, 1071–1107, 1998.

Qu, Z., Barker, H. W., Korolev, A. V., Milbrandt, J. A., Heckman, I., Bélair, S., Leroyer, S., Vaillancourt, P. A., Wolde, M., Schwarzenböck, A., Leroy, D., Strapp, J.W., Cole, J. N., Nguyen, L., and Heidinger, A.: Evaluation of a high-resolution numerical weather prediction model's simulated clouds using observations from CloudSat, GOES-13 and in situ aircraft, Q. J. Roy. Meteor. Soc., 144, 1681–1694, https://doi.org/10.1002/qj.3318, 2018.

Seifert, A. and Beheng, K.: A two-moment cloud microphysics parameterization for mixed-phase clouds. Part 1: Model description, Meteorol. Atmos. Phys., 92, 45–66, https://doi.org/10.1007/s00703-005-0112-4, 2006.

Sotiropoulou, G., Sullivan, S., Savre, J., Lloyd, G., Lachlan-Cope, T., Ekman, A. M. L., and Nenes, A.: The impact of secondary ice production on Arctic stratocumulus, Atmos. Chem. Phys., 20, 1301–1316, https://doi.org/10.5194/acp-20-1301-2020, 2020.

Sotiropoulou, G., Vignon, É., Young, G., Morrison, H., O'Shea, S. J., Lachlan-Cope, T., Berne, A., and Nenes, A.: Secondary ice production in summer clouds over the Antarctic coast: an under-appreciated process in atmospheric models, Atmos. Chem. Phys., 21, 755–771, https://doi.org/10.5194/acp-21-755-2021, 2021.

Stanford, M. W., Varble, A., Zipser, E., Strapp, J. W., Leroy, D., Schwarzenboeck, A., Potts, R., and Protat, A.: A ubiquitous ice size bias in simulations of tropical deep convection, Atmos. Chem. Phys., 17, 9599–9621, https://doi.org/10.5194/acp-17-9599-2017, 2017.

Strapp, J. W., Schwarzenboeck, A., Bedka, K., Bond, T., Calmels, A., Delanoe, J., Dezitter, F., Grzych, M., Harrah, S., Korolev, A., Leroy, D., Lilie, L., Mason, J., Potts, R., Protat, A., Ratvasky, T., Riley, J. T., and Wolde, M.: Comparisons of Cloud In Situ Microphysical Properties of Deep Convective Clouds to Appendix D/P Using Data from the High-Altitude Ice Crystals-High Ice Water Content and High Ice Water Content-RADAR I Flight Campaigns, SAE International Journal of Aerospace, 14, 127–159, https://doi.org/10.4271/01-14-02-0007, 2021.

Sullivan, S. C., Hoose, C., Kiselev, A., Leisner, T., and Nenes, A.: Initiation of secondary ice production in clouds, Atmos. Chem. Phys., 18, 1593–1610, https://doi.org/10.5194/acp-18-1593-2018, 2018.

Takahashi, T., Nagao, Y., and Kushiyama, Y.: Possible high ice particle production during graupel–graupel collisions, J. Atmos. Sci., 52, 4523–4527, https://doi.org/10.1175/1520-0469(1995)052<4523:PHIPPD>2.0.CO;2, 1995.

UCAR/NCAR – Earth Observing Laboratory: HAIC-HIWC_2015: High Altitude Ice Crystals, High Ice Water Content Project, UCAR/NCAR [data set], https://data.eol.ucar.edu/master_lists/generated/haic-hiwc_2015 (last access: 31 March 2022), 2015.

Vardiman, L.: The generation of secondary ice particles in clouds by crystal–crystal collision, J. Atmos. Sci., 35, 2168–2180, https://doi.org/10.1175/1520-0469(1978)035<2168:TGOSIP>2.0.CO;2, 1978.

Wolde, M. and Pazmany, A.: NRC dual-frequency airborne radar for atmospheric research, in: 32nd Int. Conf. on Radar Meteorology, Albuquerque, NM, 22–29 October 2005, Amer. Meteor. Soc., P1R.9, https://ams.confex.com/ams/32Rad11Meso/techprogram/paper_96918.htm (last access: 12 September 2022), 2005.